CRITICAL REVIEW

Check for updates

Electrocatalytic C–N coupling for urea synthesis: a critical review

Chuanju Yang,†[a] Zhe Li,†[b] Junpeng Xu,[c] Yujing Jiang[a] and Wenlei Zhu [ID] *[a]

Urea is one of the most important artificial nitrogen fertilizers in the agricultural economy and can provide essential nitrogen for plant growth. However, the industrial production of urea is very energy consumptive. In the past few years, the electrocatalytic approach has been regarded as a promising green approach for urea synthesis under mild conditions. Therefore, using carbon dioxide (CO_2) and nitrogenous molecules as feedstocks, electrocatalytic urea synthesis has received extensive interest and investigation. Despite the tremendous efforts that have been made, it is still very hard to significantly increase urea synthetic efficiency due to complex mechanisms. Focusing on catalyst design, characterization, electrolytic cells chosen, urea identification/quantification, determination of intermediates, and in-depth mechanisms, the recent advances in urea electrocatalytic production are summarized and discussed. Furthermore, we analyze the current challenges and prospects for the development path of electrocatalytic urea synthesis. From an application viewpoint, we hope these insights shed light on designing efficient catalysts in future studies and bring broader application prospects for green urea synthesis.

1. Introduction

Electrosynthesis methods are appealing approaches for high-value chemical production from small molecules.[1–5] By finely designing the electrocatalyst, electrochemical conversion methods can lower the energy barrier of energy-intensive processes and complete the conversions under mild conditions.[6–9] For instance, various catalysts have been introduced to facilitate electrochemical CO_2 reduction (CO_2R).[10,11] Nowadays, CO_2R reaction studies are able to reach industrialization requirements with an operating current density over 1 A cm^{-2} towards different multi-carbon products.[12,13] On the basis of CO_2R, many efforts have been made including electrochemical carbon–nitrogen (C–N) coupling methods to increase the diversity of products (*e.g.*, acetamide, urea, methylamine, formamide, *etc.*).[14] Among these organonitrogens, urea is highly anticipated since it is an excellent nutrient carrier, and

an important fertilizer in agriculture.[15,16] In addition, urea is also the indispensable feedstock for urea–melamine–formaldehyde resin, urea formaldehyde, and barbiturate synthesis.[17]

In traditional industrial manufacturing processes, urea synthesis relies on the thermal catalytic conversion of ammonium carbamate, and has made great contributions to increasing output and has driven social advancement.[18,19] However, the production of feedstock ammonia and the subsequent ammonium carbamate must overcome energy-intensive processes to break the strong bonds of nitrogen gas (N≡N, ~941 kJ mol^{-1}) and carbon dioxide (C=O, ~806 kJ mol^{-1}), respectively.[20,21] A huge amount of energy is consumed through the harsh conditions, with the emission of undesirable greenhouse gases, which is contradictory to sustainability goals.[22] Therefore, the development of green and effective electrocatalytic methods for urea synthesis is crucial for the development of human society. Benefiting from the development of advanced characterization and theoretical calculation technologies, researchers can have a better understanding of the reaction mechanism and optimize the synthetic routes of catalysts.[23] Thus, the electrocatalytic synthesis of urea is promising and has been widely investigated.

Despite the great potential of resource recovery, several challenges are still impeding the industrialization of urea electrocatalytic synthesis. Although electrosynthesis methods avoid the energy penalty and direct carbon emission from natural gas reformation, fossil fuel-based energy sources are still contrary to the conception of cleaner production. Clean, safe, and renewable energy sources are urgently needed. On

[a]*State Key Laboratory of Pollution Control and Resource Reuse, the Frontiers Science Center for Critical Earth Material Cycling, School of the Environment, Nanjing University, Nanjing 210023, People's Republic of China.*
E-mail: wenleizhu@nju.edu.cn
[b]*Nanjing Institute of Environmental Sciences, Ministry of Ecology and Environment of the People's Republic of China, Nanjing 210042, People's Republic of China*
[c]*State Key Laboratory of Pharmaceutical Biotechnology, Department of Sports Medicine and Adult Reconstructive Surgery, Nanjing Drum Tower Hospital, The Affiliated Hospital of Nanjing University Medical School; State Key Laboratory of Pharmaceutical Biotechnology, Medical School, Nanjing University, Nanjing 210093, People's Republic of China*
†These authors contributed equally to this manuscript.

the other hand, opinions are divided on the mechanism of C–N bond formation, which makes it still difficult to obtain satisfactory results with the existing electrocatalytic urea synthetic systems. A decent understanding of the in-depth factors would help scientists to develop efficient urea electrocatalytic synthesis systems. In this review, the development history of urea electrocatalytic synthesis is summarized, focusing on the key steps of the common technical schemes. Focusing on catalyst design and characterization, reactor selection, product monitoring, and mechanism investigation, the advantages and shortcomings of current reaction systems are fully discussed, and possible approaches for addressing those concerns are suggested. Finally, we analyze the requirements for realizing highly efficient urea electrocatalytic synthesis, making basic studies match the requirements of practical applications.

2. Milestones in electrocatalytic urea synthesis

The formation of C–N bonds is crucial for electrocatalytic organonitrogen synthesis. For urea, with the generation of N-nucleophilic intermediates (*NH_3, *NH_2OH, *N_2, *NO_2, *NH_2) and C-intermediates (*CO_2, *CO, *COOH, *CH_2O) on the active sites, the N-nucleophilic intermediates will attack their neighboring C-intermediates, following a configuration-stabilizing process.[24,25] Currently, accompanied by greenhouse gas CO_2, reactants such as N_2, NO_2^-, NO_3^-, NO are employed as the nitrogen sources to produce urea during the electrocatalytic process (Fig. 1). Electrocatalytic synthesis of urea was initially reported by Shibata et al. in 1995.[26] Inspired by this preliminary study, numerous reaction systems were developed and pushed electrocatalytic urea synthesis performance under ambient conditions. In 2016, Kayan et al. accomplished urea synthesis using N_2 and CO_2 as feedstocks on polyaniline

(PANI) and poly-pyrrole (PPy)-coated platinum electrodes, which could reach 7.1% FE_{urea} at −0.225 V vs. RHE.[27] In 2020, Chen et al. proposed a Pd_1Cu_1/TiO_2-400 catalyst that achieved a higher rate of urea production with a 8.92% FE_{urea} at −0.4 V vs. RHE.[28] However, the high bond energy of N_2 leads to a large over-potential, which makes the hydrogen evolution reaction occupy a dominant position in the electrocatalytic system. In response to the competitive adsorption of N_2 and CO_2 on the electrode surface, developing novel reactors and catalysts with multiple active sites is gaining more attention. In 2022, Huang and coworkers prepared Zn nanobelts (Zn NBs) by electrochemical treatment of ZnO nanosheets (ZnO NSs).[29] It is worth mentioning that the proposed system exhibits the urea yield rate of 15.13 mmol h^{-1} g^{-1}, and the corresponding FE_{urea} reached 11.26% at −40 mA cm^{-2} in a flow cell. The comprehensive utilization of nitrogen-containing molecules and CO_2 points to a possible solution for dealing with pollutant recovery and carbon neutralization in a single module.[30,31] According to the development trend in electrocatalytic urea synthesis, it is crucial to focus on byproduct inhibition and the maintenance of intermediates during the C–N coupling process. Hence, understanding the characteristics of different types of catalyst is beneficial for their subsequent design and modification.

3. Catalysts for electrochemical urea synthesis

The catalyst is of great significance in building effective reaction systems with considerable yield and faradaic efficiency.[32–36] The ideal catalyst should have exceptional capabilities for reactant capture, energy barrier management, bond cleavage, and coupling of intermediates.[37,38] Currently, the major electrocatalytic systems for urea synthesis apply metal-
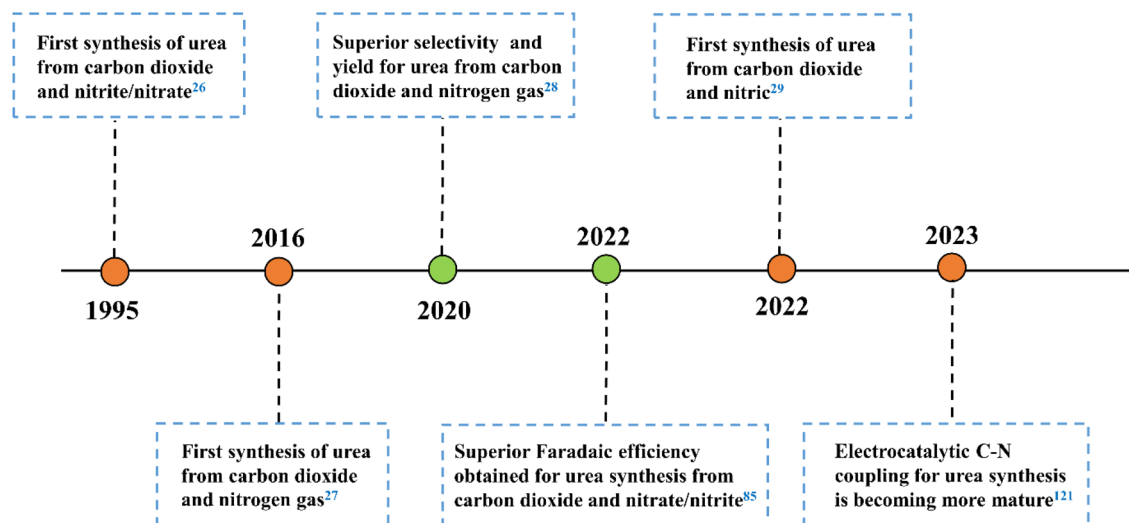

Fig. 1 The progress of C–N coupling reaction for electrocatalytic urea synthesis.

based catalysts including copper, gold, indium, *etc* (Table 1). Aiming to enhance catalytic performances, the optimization of electronic structure, coordination environment, carrier properties, and interfacial interactions are key factors to be solved. By structural engineering, catalysts can acquire unique conformational relationships to complete the complicated reactions in an easy path.[39–42]

3.1 Monometallic catalysts

Monometallic catalysts have been utilized in electrocatalytic urea synthesis processes due to their simplicity. With differentiated capabilities affecting electrocatalytic processes, monometallic catalysts with optimized metal types can be utilized in specific reactions, such as Pt (the most efficient catalyst for HER and ORR), Ir (high-efficiency catalyst for OER), and Cu (a good candidate for nitrate to ammonia production).[43–50] As aforementioned, Shibata and colleagues indicated that carbon dioxide can simultaneously reduce with nitrite/nitrate on a Cu-loaded gas-diffusion electrode to produce urea, which sets the foundation and verifies the feasibility of electrocatalytic methods in urea synthesis.[26] However, the performances of monometallic catalysts are still at a low level due to the complicated mechanisms.[51] Therefore, researchers have modified monometallic catalysts by means of structural engineering in the hope of obtaining better reaction results.

3.2 Alloy catalysts

Alloying can modify the electronic and geometric structure of the active sites, which enhances the intrinsic adsorption properties of intermediates and facilitates the formation of products.[52] Based on previous studies, nickel-based catalysts demonstrate excellent performance in the CO_2 reduction reaction (CO_2RR), while iron-based catalysts exhibit remarkable efficacy in the nitrate reduction reaction (NO_3RR).[53,54] In this case, Hou and his colleagues designed a FeNi/NC alloy catalyst for efficient urea synthesis.[55] By effectively integrating the advantages between iron-based and nickel-based catalysts, the FeNi/NC alloy catalyst shows an excellent urea yield rate of 496.5 mg h^{-1} g^{-1} and faradaic efficiency (FE) of 16.58% at −0.9 V *vs.* RHE. Wang and colleagues proposed a XC72R-AuPd electrocatalyst through the one-pot reduction of metal precursors with $NaBH_4$ (Fig. 2a).[40] The catalyst exhibits exceptional catalytic properties, with a high FE of 15.6% and excellent electrochemical stability when CO_2 and NO_3^- are used as reactants. The catalytic performance of the XC72R-AuPd outcompetes that of monometallic catalysts XC72R-Au and XC72R-Pd, which showed urea FE of 3.6% and 6.7%, respectively (Fig. 2b). They noted that a weak adsorption of CO by the catalyst would hinder the production of the active intermediate *CO, while a strong adsorption would cause catalyst poisoning. On this theoretical basis, the XC72R-AuPd electrocatalyst possesses appropriate CO adsorption capacity due to the incorporation of a small amount Pd into Au nanocrystal. Moreover, this also leads to a thermodynamically spontaneous C–N coupling between *NH2OH and *CO, which is in favor of the formation of urea (Fig. 2c). Liu and his colleagues fabricated an AuCu

self-assembled nanofiber (AuCu SANF) *via* the hydrothermal method, coupling CO_2R with nitrite reduction (NO_2R) for urea electrosynthesis (Fig. 2d and e).[56] The AuCu SANFs showcased excellent urea synthesis performance, achieving a high urea faradaic efficiency of 24.7% at −1.45 V *vs.* RHE (Fig. 2f). Also, the proportions of Au and Cu in SANF had an impact on the urea faradaic efficiency. Furthermore, the authors revealed that AuCu SANFs could modulate the coordination state and electronic structure of Au and Cu, which facilitated the adsorption and activation of reactants (CO_2, NO_2^-). Feng and coworkers prepared the Te-doped Pd nanocrystal (denoted as Te–Pd NC) by a wet-chemical approach (Fig. 2g).[57] The electrochemical synthesis of urea was achieved with nearly 12.2% faradaic efficiency at −1.1 V *vs.* RHE, much higher than those of Pd NCs (Fig. 2h). According to mechanism studies and theoretical calculations, doping with Te promotes the formation of *CO and eliminates active sites that strongly adsorb CO, which results in the Te-doped Pd nanocrystal exhibiting a higher stability against CO poisoning (Fig. 2i). The synergy between Te and Pd in Te–Pd NCs significantly promotes the transformation of CO_2 to *CO and NO_2^- to *NH2, which facilitates the binding between *CO and *NH2 (Fig. 2j and k).

The study and preparation of alloy catalysts mostly rely on the interaction of two metals. Although the preparation and evaluation of alloy electrocatalysts have progressed significantly, their size, composition, and active site control still lack a reliable method to control. Furthermore, the structural relationships of alloy electrocatalysts are still not thoroughly researched. As a result, sophisticated theoretical calculations and modelling methods are necessary to achieve catalytic co-production of urea. In addition, considering the high costs of using metal precursors for metallic and alloy catalyst synthesis, functional atomic catalysts with lower precursor utilization have received much attention in recent decades.[58,59]

3.3 Single-atom structures

The smaller size means the existence of more low-coordinated metal atoms with catalytic activity, leading to a higher specific activity (SA).[60] Owing to the low cost, minimal metal usage, large surface areas, and high activity, single-atom catalysts (SACs) have recently garnered attention in energy conversion reactions.[61] In SACs, around the active center, the localized ligands impact the activity, stability, and selectivity. With a lone pair of electrons, ligands can trap isolated metal centers and regulate their electronic structure.[62,63] Over the past few years, SACs have been well developed in the electrochemical carbon dioxide reduction (ECR) system and nitrogenous species reduction reaction (NRR).[64] According to the existing research bases, using single-atom catalysts to realize electrocatalytic urea synthesis has been further investigated. For instance, Leverett *et al.* distributed Cu single atoms on a nitrogen-doped carbon substrate to form Cu–N_x–C_x *via* hydrothermal methods (Fig. 3a).[65] As the pyrolysis temperature increases from 800 °C to 1000 °C, the coordination structure changes from Cu–N_4 sites to Cu–N_3–C_1 and Cu–N_2–C_2 sites (Fig. 3b). The configuration of Cu–N_x–C_x plays a vital role in
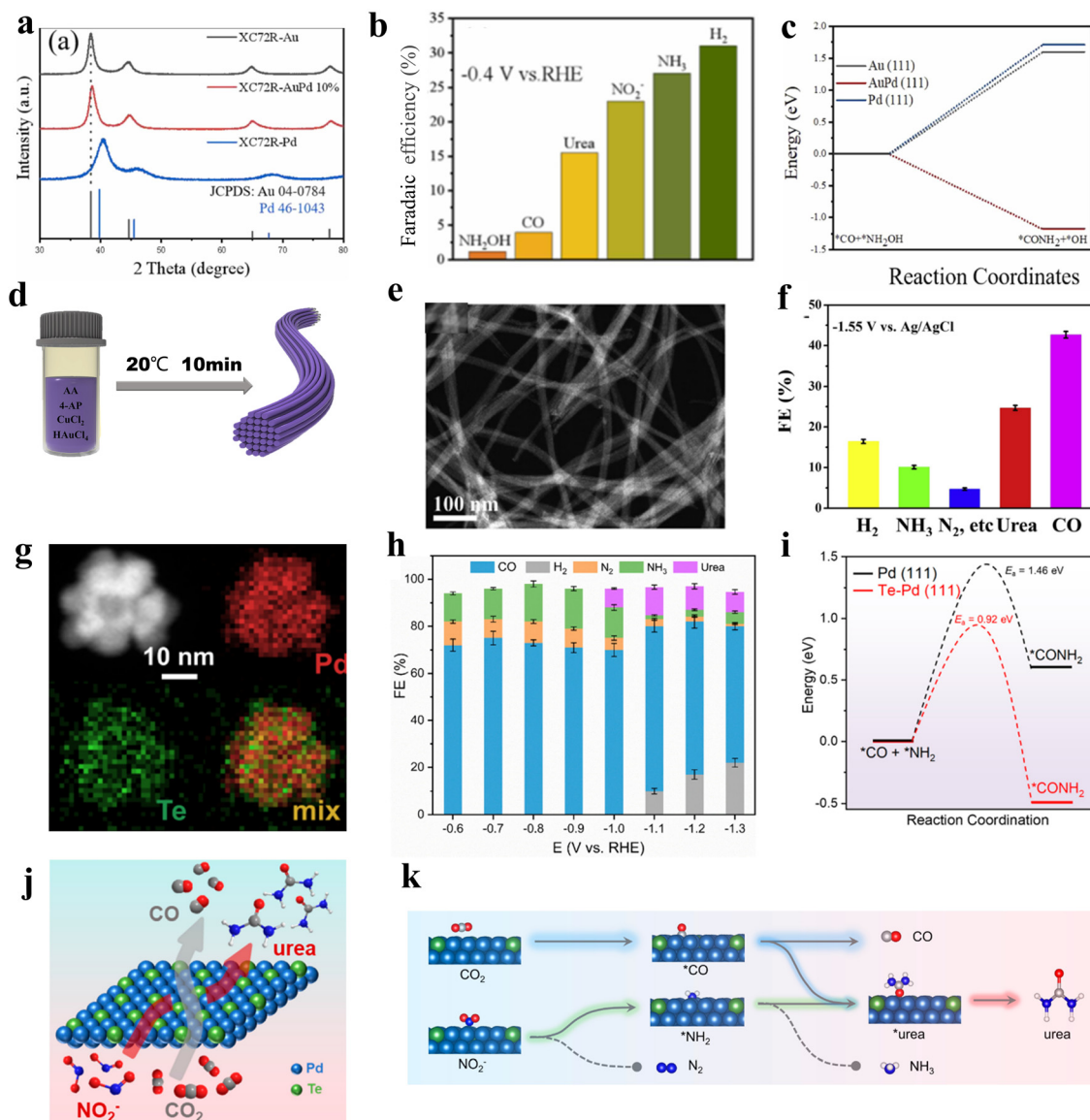
Fig. 2 (a) XRD patterns of XC72R-AuPd samples. (b) Faradaic efficiencies for different products by using XC72R-AuPd at −0.4 V *vs.* RHE in H-cell. (c) Free energies for *CO + *NH$_2$OH → *CONH$_2$ on Au, AuPd, and Pd. Reproduced from ref. 40, with permission from Elsevier, copyright 2022. (d) The fabrication of the AuCu SANFs. (e) HAADF-STEM images of AuCu SANFs. (f) Faradaic efficiencies for different products by using AuCu SANFs at −1.55 V (*vs.* Ag/AgCl) in H-cell. Reproduced from ref. 56, with permission from Elsevier, copyright 2022. (g) HAADF-STEM image and corresponding elemental mappings of Te−Pd NCs. (h) Faradaic efficiencies for different products by using Te−Pd NCs/C in H-cell. (i) Free energy changes and activation barriers of *CONH$_2$ on the Te−Pd (111) surface and pure Pd (111) surface, respectively. (j) A schematic depicts urea formation from simultaneous electroreduction of CO$_2$ and NO$_2^-$. (k) Urea synthesis from CO$_2$RR and NO$_2$RR on Te−Pd NCs. Reproduced from ref. 57, with permission from American Chemical Society, copyright 2020.

directing CO$_2$R and NO$_3$R reactions. When using CO$_2$-saturated KHCO$_3$ as the electrolyte, the FE$_{Cu-N4}$ for CO reaches 59% at −0.8 V *vs.* RHE, which is higher than that of Cu–N$_3$–C$_1$ and Cu–N$_2$–C$_2$. On the other hand, Cu–N$_2$–C$_2$ prefers to carry out NO$_3$RR at similar potentials. It is noteworthy that, when introducing NO$_3^-$ into the electrolyte of CO$_2$RR, Cu–N$_4$ reaches a 28% faradaic efficiency for urea production at −0.9 V *vs.* RHE, which is higher than Cu–N$_3$–C$_1$ and Cu–N$_2$–C$_2$ (Fig. 3c). DFT calculations reveal comparable energy barriers for C–N bond formation from *CO and *NH$_2$ on each coordination

structure (Fig. 3d). The key to unlocking exceptional CO$_2$RR performance lies in the undercoordinated N atoms that surround isolated Cu species. These N atoms can strongly interact with CO$_2$, resulting in a significant enhancement of the overall CO$_2$RR process. Thus, CO$_2$RR exhibits greater favorability on Cu–N$_4$ sites, resulting in greater urea yield on those sites. However, remarkable CO$_2$ reduction capacity does not always relate to satisfactory urea synthesis performance; the equilibrium between CO$_2$RR and NO$_3$RR is the key to achieving the ideal state of urea synthesis. Wei *et al.* fabricated a Cu single-
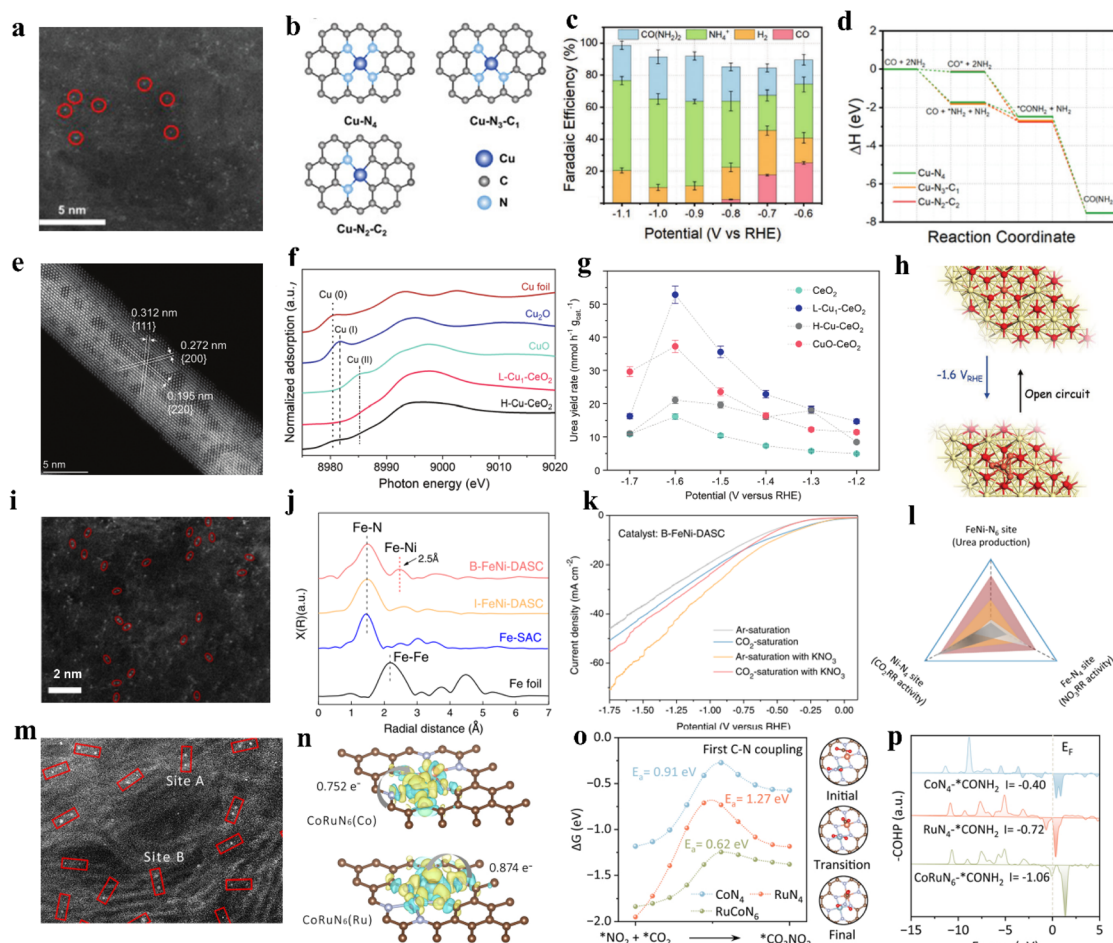
Fig. 3 (a) HAADF-STEM image of Cu-GS-800. (b) Graphical representations of modeled Cu−N$_x$−C$_x$ sites. (c) Faradaic efficiencies for different products by using Cu-GS-800 in H-cell. (d) Reaction pathway for urea production from simultaneous CO$_2$RR and NO$_x$RR. Reproduced from ref. 65, with permission from Wiley-VCH, copyright 2022. (e) AC-HAADF-STEM image of L-Cu$_1$-CeO$_2$. (f) XANES image of L-Cu$_1$-CeO$_2$. (g) The urea yield rates of CeO$_2$, L-Cu$_1$-CeO$_2$, H-Cu-CeO$_2$, and CuO−CeO$_2$ catalysts at different applied potentials. (h) Schematic diagram of reconstitution of copper single-atoms to clusters suggested by the *operando* XAS measurements. Reproduced from ref. 66, with permission from Wiley-VCH, copyright 2023. (i) Aberration-corrected HAADF-STEM image of B-FeNi-DASC. (j) Fourier transform extended X-ray absorption fine structure (FT-EXAFS) spectra of Fe-SAC, I-FeNi-DASC, and B-FeNi-DASC. (k) LSV curves of B-FeNi-DASC. (l) Correlations between CO$_2$RR activity, NO$_3$RR activity, and urea production over various site configurations. Reproduced from ref. 76, with permission from Springer Nature, copyright 2022. (m) HAADF-STEM image of CoRuN$_6$. (n) Charge density differences of Co and Ru in CoRuN$_6$ simulated structure. (o) The reaction pathway of first C−N coupling for *CO$_2$NO$_2$ formation. (p) The crystal orbital Hamilton population (COHP) of *CONH$_2$ intermediate onto CoN$_4$, RuN$_4$ and CoRuN$_6$. Reproduced from ref. 77, with permission from Elsevier, copyright 2023.

atom catalyst on a CeO$_2$ support (Cu-CeO$_2$) through the wet impregnation and calcination method.[66] Catalysts were labeled L-Cu$_1$-CeO$_2$ and H-Cu$_1$-CeO$_2$ based on the concentration of impregnated copper. They found copper was atomically dispersed in L-Cu$_1$-CeO$_2$, while the H-Cu$_1$-CeO$_2$ surface was distributed with numerous copper clusters and nanoparticles (Fig. 3e and f). As a result, the L-Cu$_1$-CeO$_2$ exhibits a urea yield rate of 52.84 mmol h^{-1} g^{-1} at −1.6 V *vs.* RHE, which is higher than that of CeO$_2$ and H-Cu$_1$-CeO$_2$ (Fig. 3g). Based on the *in situ* X-ray absorption spectroscopy (XAS) results, Cu single atoms tend to form Cu clusters during the electrocatalytic process, and will recover to the single-atom state at open circuit voltage (OCV) (Fig. 3h). To identify whether the urea yield rate is related to the copper active sites or the electronic

structure changes of Cu-CeO$_2$, various metal-CeO$_2$ single-atom structures have also been investigated. According to the experimental results, the performance of the Cu$_1$-CeO$_2$ structure is significantly superior to other M$_1$-CeO$_2$ structures. Through the projected density of states (PDOS) of adsorbed NO$_3^-$ and CO$_2$ on the M$_1$-CeO$_2$ catalysts, it was indicated that only Cu−O bonds offer uniquely hindered Lewis acid–base active sites that can realize efficient urea synthesis on Cu$_1$-CeO$_2$.

Unfortunately, urea synthesis through single-atom catalyst methods has received much less attention compared with the research on CO$_2$RR and NRR. Meanwhile, competing reactions on the active sites can lead to slow rates of certain reactions and ultimately result in low urea yields, similar to monometallic catalysts. Efficient atom catalysts for urea synthesis should

be developed, building upon the research on CO$_2$RR and NRR. Zn-SACs, Fe-SACs, and Ni-SACs have been proved to be efficient CO$_2$RR electrocatalysts.[67–69] Ru SAs/N–C, Fe–N–C, and Mo/GDY have also been demonstrated as effective NRR electrocatalysts.[70–72] Combining the advantages of single-atom catalysts in single reactions, the development of diatomic catalysts is gaining more and more attention as a strategy to overcome the inherent drawbacks of single-atom catalysts and enhance the reaction efficiency.

3.4 Dual-atom structures

Typically, diatomic catalysts allow two metal atoms to interact and stabilize in a restricted domain, while increased metal loading provides more active centers, meaning that catalytic performance is also improved.[73] Such a catalyst usually has better activity than single-atom ones, as well as the faradaic efficiency, selectivity, and stability of target reactions. This leads to a synergy greater than the simple sum of parts, achieving "1 + 1 > 2".[74] Furthermore, the reactions on dual-atom structures are conducive to realizing simultaneous generation of C and N-intermediates on active sites. Therefore, the construction of the dual-atom structure plays a crucial role in urea synthesis.[75] Wang and coworkers designed a diatomic catalyst (DAC) with bonded Fe–Ni (B-FeNi-DASC) pairs through pyrolysis of the coordination polymer (Fig. 3i and j).[76] Compared with Fe-SAC, Ni-SAC, and I-FeNi-DASC electrocatalysts, B-FeNi-DASC demonstrated a better urea synthesis performance by achieving a high urea yield of 20.2 mmol h^{-1} g^{-1} with a corresponding faradaic efficiency of 17.8%. Notably, the faradaic efficiency of CO, as for NH$_3$, showed diametrically opposed results when using Fe-SAC or Ni-SAC as electrocatalyst: the highest FE$_{CO}$ of Fe-SAC and Ni-SAC is 86.9% and 19.2%, while the highest FE$_{NH_3}$ of Fe-SAC and Ni-SAC is 19.9% and 65.2%, respectively. Apparently, single-atom systems present inherent disadvantages in handling intricate catalytic reactions that involve multiple reactants and intermediates. Despite the fact that I-FeNi-DASC with isolated diatomic sites Ni–N$_4$ and Fe–N$_4$ can activate multiple C and N species, it is unable to generate enough intermediate species without the creation of efficient C–N coupling sites. Remarkably, B-FeNi-DASC, introduced with Fe–Ni pairs in the form of FeNi-N$_6$ configuration, can exhibit a synergistic effect and accelerate the reaction kinetics of the C–N coupling process. Furthermore, the thermodynamic and kinetic processes involved in C–N bond formation were also enhanced (Fig. 3k and l). Liu and coworkers designed Co–Ru dual-atom anchored N-doped carbon (CoRuN$_6$) by the coordination and calcination method.[77] As shown in the high-angle annular dark field scanning transmission electron microscopy (HAADF-STEM) image, numerous bright spots of Ångstrom size are evenly distributed on the carbon matrix and mainly appeared in pairs (Fig. 3m and n), which indicates the Co and Ru sites were dispersed in atomic form instead of becoming clusters. The diatomic asymmetric system successfully achieves high urea yield and selectivity by inhibiting parallel reactions (Fig. 3o and p). Consequently, the CoRuN$_6$ electrocatalyst exhibited a urea yield rate of 8.98 mmol h^{-1} g^{-1}

with a faradaic efficiency of 25.31% at −0.6 V vs. RHE. In contrast with single-atom catalysts, the selectivity of NH$_3$ and CO byproducts was decreased on CoRuN$_6$ (37.99% and 6.4%, respectively), which favored C and N-intermediates' participation in the C–N coupling process.

Current reports for DACs synthesis have mainly focused on atomic layer deposition (ALD), wet chemisorption, and high-temperature thermal treatment methods.[78–81] However, while DACs have been intensively studied and applied, preparing highly dispersed DACs remains a significant challenge, because of the inevitable aggregation of metal atoms during the synthesis process. In addition, when using DACs in electrocatalytic urea synthesis, the accurate identification of active sites in DACs is an issue that needs further investigation.

3.5 Vacancy defects

Vacancy engineering is crucial in adjusting target reactions since the vacancies can effectively modify the electronic structure of catalysts and tune the adsorption features of CO$_2$, nitrogen feedstocks and intermediates.[75,82] For instance, oxygen vacancy (V$_O$) is an important structural defect in metal oxides that can serve as catalytic centers with rich electron densities.[83,84] Lv and colleagues fabricated V$_O$-InOOH electrocatalyst via a facile solvothermal method. The defect-engineered catalyst delivers a 51% FE$_{urea}$ at −0.5 V vs. RHE.[85] In contrast, InOOH electrocatalysts with no V$_O$ exhibited lower electrocatalytic performance with a 26.3% FE$_{urea}$. After the long-term (24 h) chrono-amperometry test and five successive cycles of electrocatalysis, V$_O$-InOOH displayed no obvious degradation in catalytic performance. It was also confirmed that oxygen vacancies conferred more surface electrons to In (OOH). These surface electrons are further transferred to the surface adsorbed CO$_2$, which leads to a thicker accumulation of holes than the InOOH, and inhibits HER by repelling protons in the electrolyte. Wei and colleagues proposed a series of V$_O$-enriched CeO$_2$ nanorods to investigate the effects of V$_O$ concentration on the properties of catalysts (Fig. 4a).[86] V$_O$-CeO$_2$-750 with the highest vacancy concentration exhibits a urea yield rate of 943.6 mg h^{-1} g^{-1}, superior to that of partial noble-metal-based electrocatalysts. Interestingly, the active sites of V$_O$-CeO$_2$-750 were occupied by nitrate reduction, which was confirmed by the greatly reduced CO formation rate in co-electrolysis. However, in either nitrate reduction or C–N coupling processes, V$_O$-CeO$_2$-750 shows lower ammonia yield rates (Fig. 4b and c). Based on the existing data, the authors propose that V$_O$ stabilizes N-containing intermediates and exceeds their hydrogenation, thus facilitating the C–N coupling process and subsequent urea formation (Fig. 4f). Meng and coworkers prepared ZnO-V$_O$ porous nanosheets via electrodeposition.[87] When using NO$_2^-$ as the N-source, the ZnO-V$_O$ porous nanosheets exhibit an optimized FE$_{urea}$ of 23.26% at −0.79 vs. RHE, which is almost three times that of ZnO porous nanosheets. Through a series of controlled experiments, they confirmed the competitive relationship between CO$_2$RR and NO$_2$RR on ZnO-V$_O$. Due to the existence of more active sites in ZnO-V$_O$, the efficiency of urea generation is greatly promoted.
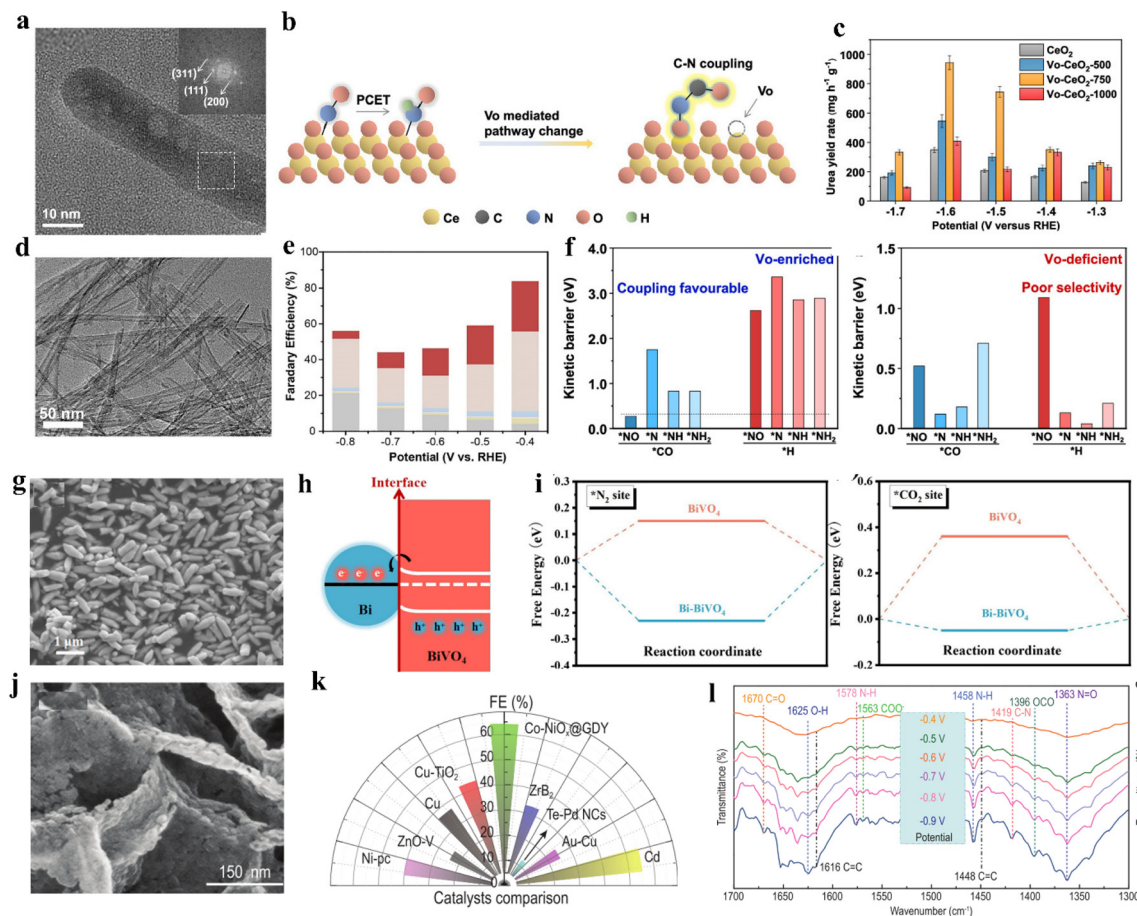
Fig. 4 (a) TEM and HAADF-STEM images of Vo-CeO$_2$-750. (b) Schematic diagram of Vo-mediated reaction pathway changes on CeO$_2$. (c) Urea yield rates of CeO$_2$, Vo-CeO$_2$-500, Vo-CeO$_2$-750, and Vo-CeO$_2$-1000 at various applied potentials. Reproduced from ref. 86, with permission from American Chemical Society, copyright 2022. (d) HRTEM images of Cu-TiO$_2$ samples. (e) Faradaic efficiencies of major reduction products for Cu-TiO$_2$ catalysts. Reproduced from ref. 89, with permission from Elsevier, copyright 2020. (f) Comparison of the energy barriers for C–N coupling of *NO, *N, *NH, and *NH$_2$ with *CO and protonation on Vo-enriched CeO$_2$ and Vo-deficient CeO$_2$. (g) SEM image of Bi-BiVO$_4$ hybrids. (h) Schematic illustration of the charge transfer process in Bi-BiVO$_4$ (i) N$_2$ and CO$_2$ adsorption on BiVO$_4$ and Bi-BiVO$_4$; the bottom figures are the corresponding calculation models. Reproduced from ref. 94, with permission from Wiley-VCH, copyright 2021. (j) High-magnification SEM images of Co-NiO$_x$@GDY. (k) Comparison of the FE value of Co-NiO$_x$@GDY with reported catalysts. (l) Infrared signals in the range of 1700–1300 cm^{-1}. Reproduced from ref. 98, with permission from Oxford University Press, copyright 2022.

It is well known that copper (Cu)-based materials have notable performances in CO$_2$RR and NO$_3$RR; the combination of Cu and V$_O$-rich materials also provides an alternative catalyst for electrocatalytic urea synthesis.[82,88] Cao and colleagues provided Cu-doped oxygen vacancy-rich anatase TiO$_2$ (Cu-TiO$_2$) nanotubes for the electrochemical co-reduction of both CO$_2$ and NO$_2^-$, giving a FE$_{urea}$ of 43.1% at −0.4 V vs. RHE (Fig. 4d and e).[89] Low-valence Cu doping induces abundant oxygen vacancies due to its unique d-electronic nature, favoring the exposure of bi-Ti^{3+} active sites. The oxygen vacancies in the proposed system provide more adsorption sites, facilitating the C–N coupling reaction.

A suitable amount of oxygen vacancies can provide more active sites and stabilize intermediates in C–N coupling reactions by modifying the energy level, conductivity, and molecular adsorption properties of the catalysts.[90,91] A thorough understanding of vacancies can provide valuable insights for

designing novel electrocatalysts. In future applications, with the development of preparation methods, new insights can be provided for vacancy engineering to improve the performance of urea synthesis systems.

3.6 Heterogeneous structures

Heterojunction catalysts play an important role in novel catalysts. In heterojunction catalysts, electrons can be rearranged at the heterostructure interface to modify the active sites. The synergistic effect between the active sites is conducive to promoting the reaction kinetics.[92,93] Yuan and colleagues prepared Mott–Schottky heterostructure Bi-BiVO$_4$ hybrids by the NaBH$_4$ reduction strategy (Fig. 4g).[94] When introducing N$_2$ and CO$_2$ as feedstocks, the proposed system delivers a urea production rate of 5.91 mmol h^{-1} g^{-1} with a FE$_{urea}$ of 12.55% at −0.4 V vs. RHE (Fig. 4h and i). In contrast, the electrochemical performances of pristine BiVO$_4$ are significantly decreased. As

the study mentioned, Bi-BiVO$_4$ can form a Mott–Schottky heterostructure and a space charge region can occur due to the electron transfer from BiVO$_4$ to metallic Bi. The unique structure greatly enhances the chemisorption capability of inert N$_2$ and CO$_2$ molecules, which is a prerequisite for the efficient synthesis of urea. Meanwhile, Bi-BiVO$_4$ can effectively suppress the generation of C or N by-products, which leads to satisfactory urea production. By utilizing a similar mechanism, Yuan and colleagues put forward perovskite-structured BiFeO$_3$/BiVO$_4$, with FE$_{urea}$ up to 17.18% at −0.4 V *vs.* RHE in 0.1 M KHCO$_3$, which is also higher than the pristine BiFeO$_3$ and BiVO$_4$.[95] BiFeO$_3$/BiVO$_4$ hybrids endow the surfaces of BiFeO$_3$ and BiVO$_4$ with local nucleophilic and electrophilic regions and is beneficial for the adsorption of CO$_2$ and N$_2$ molecules. Graphdiyne (GDY) has several unique characteristics, including non-uniform surface charge distribution, infinite natural pores, and good stability.[96,97] Zhang and colleagues indicated that the *in situ* growth of a multi-heterojunction interfacial structure can facilitate the intermediates' adsorption/desorption capacity and suppress side reactions (Fig. 4j). As a result, the as-prepared Co-NiO$_x$@GDY demonstrated a high urea yield rate of 913.2 mg h^{-1} g^{-1} and improved faradaic efficiency of 64.3% at −0.7 V *vs.* RHE by the co-reduction of CO$_2$ and NO$_2^-$ (Fig. 4k and l).[98]

An increasing number of strategies have been applied for constructing heterogeneous structures, including thermal treatment, hydrothermal synthesis, electrodeposition, and ion exchange methods.[99–101] However, the heterojunctions in catalysts are still not well parsed and their characterization is also limited. Relatively low current density and faradaic efficiency limit the further application of heterojunction catalysts, so their in-depth theoretical exploration needs to be further investigated.

3.7 Heteroatom doping

Heteroatom doping gives a chance to modify the electronic structure of the catalyst, optimize the intermediate binding strength, and enhance the reaction kinetics.[102] In general, heteroatom doping can be divided into two categories according to atom types: metallic doping and non-metallic doping.[103] Benefiting from the high electronegativity of non-metallic material, the surrounding atoms are easily polarized. Thus, non-metallic doping can change the electron density and shift the d-band center of the active sites to promote electrocatalytic reactions.[104] In the study of non-metallic-based catalysts, doping carbon materials with heteroatoms (*e.g.*, N, B, and F) is considered an efficient strategy to optimize the catalytic performance.[105–107] Liu and colleagues proposed carbon nanotubes with a fluorine-rich surface (F-CNT), which achieved a urea yield rate up to 6.36 mmol h^{-1} g^{-1} with FE$_{urea}$ of 18% at −0.65 V *vs.* RHE, 3.8 times higher than the pristine CNT (1.66 mmol h^{-1} g^{-1}).[108] DFT calculation indicates the F-doped graphite shell provides the active sites ("C–F$_2$ moieties") for electrocatalytic urea synthesis. Large electronegativity of F-dopants leads to stronger charge-transfer, and effectively suppresses the activity of HER. Therefore, when F-dopants are

combined with the intact CNT inner walls with high efficiency charge transfer and good conductivity, the F-CNT catalyst shows outstanding urea synthesis performance. Additionally, Mo-based materials have also emerged as promising electrocatalysts for energy storage. Jiao and colleagues put forward a catalyst containing MoP-(101) surface, which achieved the urea yield rate of 12.4 mg h^{-1} g^{-1} with 36.5% FE$_{urea}$.[109] They deemed that the incorporation of P will induce electron transfer from Mo to P, leading to a moderate coupling between Mo-d and P-p orbitals. Therefore, the surface Mo atoms can realize the coexistence of empty and occupied d orbitals. By means of DFT calculation, they revealed that the exposed Mo active sites in the MoP-(101) surface exhibit high reactivity towards the simultaneous activation of N$_2$ and CO$_2$, which facilitates the formation of characteristic C and N intermediates to generate urea in the operating system. Zhu and colleagues synthesized CuB$_{12}$ monolayer to realize urea production in an electrocatalytic system.[110] The empty and occupied p orbitals of non-metallic B can efficiently adsorb and activate the inert N$_2$ molecule. On the other hand, the electron-deficient B atom can also adsorb and activate the inert CO$_2$ by providing electrons to CO$_2$ and breaking the inherent p bond.

The degree of electronic modulation induced by the doping of heteroatoms in catalytic materials varies depending on the electronegativity and size of the dopant atoms as well as the type of dopant that ultimately forms the atoms.[111] However, there are significant discrepancies between theoretical modeling simulations and practical results. The atoms' interaction and the exact catalytic mechanism remain underexplored. A synthetic method that can provide a variety of heteroatom-doped catalysts to achieve high doping density and uniform distribution of multi-element doping is still lacking.[112]

3.8 Other catalysts

Facet-dependent selectivity was first proposed by Hori *et al.* in 1995.[113] Recently, Lv and colleagues synthesized In(OH)$_3$-S with well-defined (110) facets by a solvothermal method (Fig. 5a).[41] To highlight the role played by facets on In(OH)$_3$-S (110) in boosting urea production, the control experiments were also conducted on In(OH)$_3$-M with mixed facets of (110) and (111). By using In(OH)$_3$-S, the urea yield reached 533.1 mg h^{-1} g^{-1} with a 53.4% FE$_{urea}$ at −0.6 V *vs.* RHE. In contrast, In(OH)$_3$-M reported a lower urea yield of 392.6 mg h^{-1} g^{-1} with 34.6% FE$_{urea}$ (Fig. 5b). The authors indicated that CO$_2$ can capture the electrons to introduce a hole accumulation layer on the surface of the In(OH)$_3$-S. The hole accumulation layer can restrict protons from approaching In(OH)$_3$-S, which plays the dominant role in impeding HER on In(OH)$_3$-S (Fig. 5c). However, the electron holes on In(OH)$_3$-M (111) facets are combined with electrons from (110) facets, which weakens HER suppression. Besides, DFT calculation indicates that the transformation of NO$_3^-$ to *NO$_2$ intermediate is spontaneous kinetically and thermodynamically. This led to the higher coverage of *NO$_2$ and the inhibition of CO$_2$RR on the surface of In(OH)$_3$-S. However, the *NO$_2$ on In(OH)$_3$-M is in weak adsorption, which is unfavorable to the formation of *CO$_2$NO$_2$. On

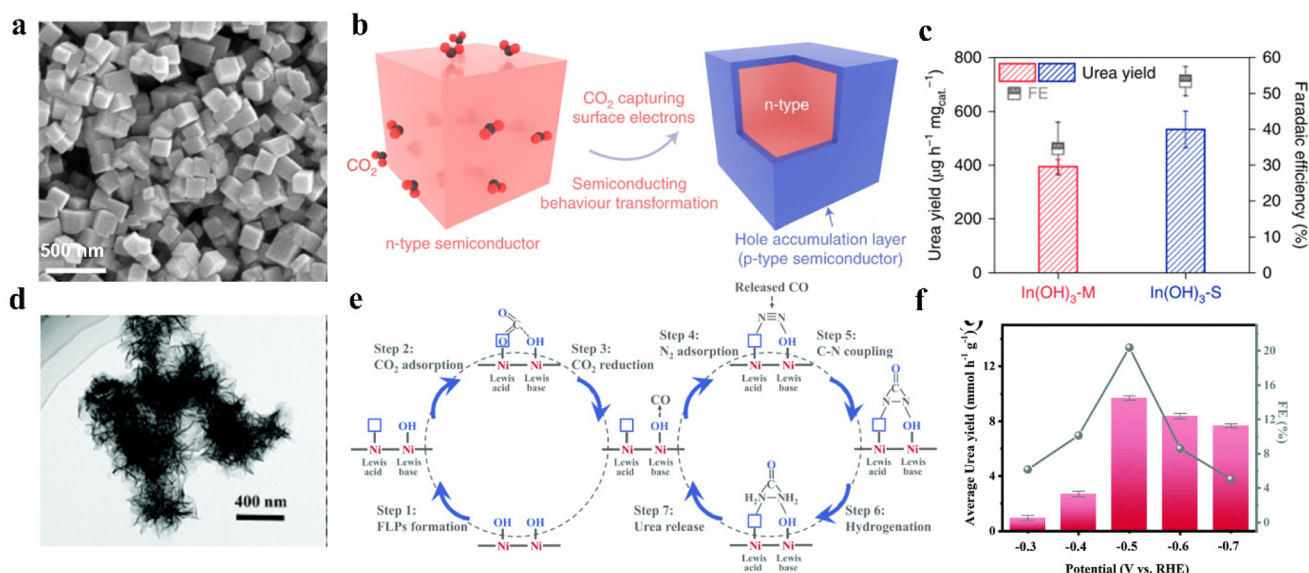**Fig. 5** (a) SEM image of In(OH)$_3$-S. (b) CO$_2$ capture induced n-type In(OH)$_3$ structure transformation. (c) Urea synthesis performance of In(OH)$_3$-S and In(OH)$_3$-M at −0.6 V *vs.* RHE. Reproduced from ref. 41, with permission from Springer Nature, copyright 2021. (d) HRTEM images of Ni$_3$(BO$_3$)$_2$-150 catalysts. (e) Schematic illustration of the electrocatalytic co-activation of N$_2$ and CO$_2$ into urea over artificial frustrated Lewis pairs (FLPs) of Ni$_3$(BO$_3$)$_2$-150 catalysts. (f) Faradaic efficiency for urea by using Ni$_3$(BO$_3$)$_2$-150 catalysts in H-cell. Reproduced from ref. 116, with permission from Royal Society of Chemistry, copyright 2021.

the other hand, the (110) facets possess relatively adjacent indium atoms to endow catalysts with favorable platforms for constructing the In–O–C–O–In configuration. Such a configuration can stabilize the adsorption of *CO$_2$, which lowers the energy barrier toward C–N coupling.

Lewis acid–base theory states that Lewis acids (LA) always have empty orbitals and the capability to form coordination bonds with Lewis bases (LB) containing lone electron pairs.[114] Generally, the unsaturated metal sites act as the LA and the metal hydroxyl groups serve as the LB.[115] For instance, Yuan and colleagues prepared Ni$_3$(BO$_3$)$_2$-150 through a facile wet chemical strategy followed by low-temperature annealing (Fig. 5d).[116] The catalyst realized an excellent urea yield rate of 9.70 mmol h^{-1} g^{-1} with a 20.36% FE$_{urea}$ at −0.5 V *vs.* RHE (Fig. 5e). In contrast with Lewis acidic Ni$_3$(BO$_3$)$_2$-250 and Lewis basic Ni$_3$(BO$_3$)$_2$, the flower-like Ni$_3$(BO$_3$)$_2$-150 has frustrated Lewis pairs (FLPs) and unsaturated Ni sites. The existence of FLPs and unsaturated Ni sites makes Ni$_3$(BO$_3$)$_2$-150 able to introduce effective absorption of CO$_2$ and N$_2$, and facilitate the spontaneous coupling of *NN* and *CO to generate the desired *NCON* (Fig. 5f).

The rational design and optimization of catalysts is a critical link in achieving the efficient electrocatalytic production of urea. At present, the competitive reaction on active sites and stabilization of C and N intermediates during the reaction process remain a hot spot during catalyst design. In addition to improving catalytic performance, it is also crucial to optimize the stability of the catalyst in consideration of future applications. Unstable behaviors, such as aggregation, exfoliation, and electronic structure changes of the catalyst may lead

to a decrease in current density and Faraday efficiency. The visual characterization of catalysts enables us to get a better understanding of catalyst properties and facilitate the technological innovation of catalyst design.[117]

4. Catalyst characterization

The morphology, lattice structure, coordination environments, and surface chemical states are essential for gaining insights into the catalyst structure and reaction mechanism. In this section, characterization techniques for catalysts are summarized and classified.

4.1 Microscopic methods

Electron microscopes have become an indispensable tool for characterizing the morphology, crystallography, composition and electronic properties of electrocatalysts at the nanoscale.[118] In addition to scanning electron microscopy (SEM) and transmission electron microscopy (TEM), high-resolution transmission electron microscopy (HRTEM) and high-angle/medium-angle annular dark field scanning transmission electron microscopy (HAADF-STEM) also play important roles in morphology characterization.[14,119,120] The atomic-level resolution of HRTEM has enabled clear observation of crystal internal structure, atomic arrangement, and fine structures for most catalysts (Fig. 6a and b).[121] HAADF-STEM is a powerful tool to study the atomic number with higher spatial resolution. A suitable microscopic method is conducive for us to gain an
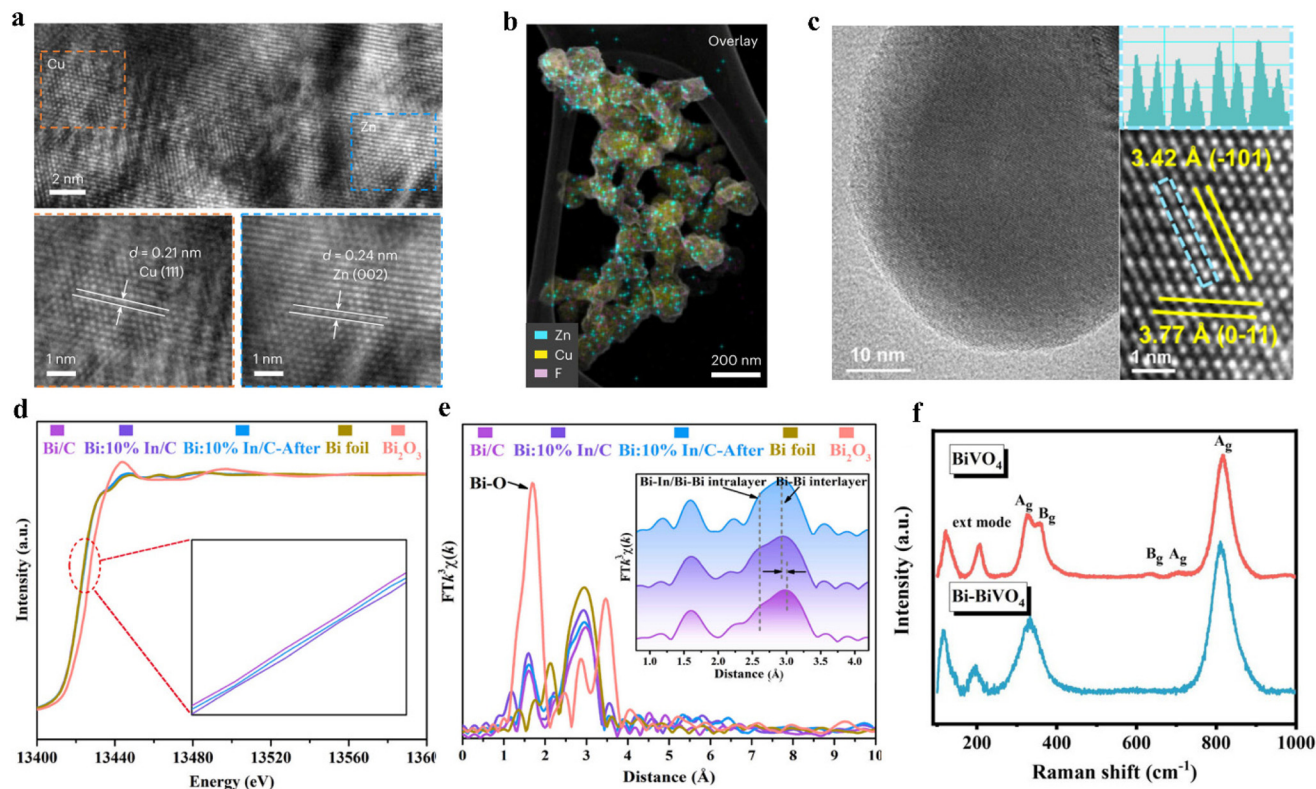
Fig. 6 (a) HR-TEM image and the corresponding element mapping of 3D Zn/Cu hybrids. (b) The uniform deposition of Zn on Cu. Reproduced from ref. 121, with permission from Springer Nature, copyright 2023. (c) TEM and atomic-resolution HAADF-STEM image with line profile of the CuWO$_4$. Reproduced from ref. 122, with permission from Springer Nature, copyright 2023. (d) The normalized XANES spectra at the Bi L$_3$-edge of Bi/C, Bi:10%In/C, Bi:10%In/C after testing, Bi foil and Bi$_2$O$_3$. (e) R space and corresponding inverse FT-EXAFS results of Bi/C, Bi:10%In/C, Bi:10%In/C after testing, Bi foil and Bi$_2$O$_3$. Reproduced from ref. 125, with permission from Royal Society of Chemistry, copyright 2021. (f) Raman spectra of BiVO$_4$ and Bi-BiVO$_4$. Reproduced from ref. 116, with permission from Royal Society of Chemistry, copyright 2021.

in-depth understanding of the fine structure of the designed catalyst, and provide ideas for catalyst modification (Fig. 6c).[122]

4.2 Spectroscopic methods

Spectroscopic characterization is crucial for identifying the coordination environment and the chemical surface states of materials. For instance, X-ray absorption spectroscopy (XAS) is a cutting-edge technique for detecting the local electronic and atomic structure of electrocatalysts, and encompasses extended X-ray absorption fine structure (EXAFS) and X-ray absorption near-edge structure (XANES).[123] XANES is able to provide detailed information on catalysts including the geometry, state, and electronic structure of absorbing atoms. EXAFS is typically used to provide information on the concentration, type, and distance to the ligands of the absorbing element and neighboring atoms.[124] For example, Mao and his colleagues performed XAS analysis on the Bi:10%In/C during the C–N coupling process.[125] Through the XANES method, they found that the spectra of the three samples (Bi/C, Bi:10%In/C, Bi:10%In/C after testing) almost overlap with the Bi foil, indicating that the Bi species are in the Bi^0 state. In comparison with Bi/C, the absorption threshold position of Bi:10%In/C slightly shifts to a higher energy, indicating that Bi is in an

electron-deficient state after the introduction of In (Fig. 6d). After the introduction of In, the Fourier transforms of the Bi L$_3$-edge EXAFS show that the interlayer Bi–Bi bond shifts towards a reduced bond length. This promoted the delocalization of Bi p-electrons and enhanced the adsorption and activation of reactive species (Fig. 6e).

Raman spectroscopy provides a unique strategy for identifying the chemical characteristics of molecular features. It enables the investigation of surface adsorbates and intermediates, as well as the monitoring of structural parameters on the catalyst surface.[126] It can detect diverse vibration patterns in group states and chemical bonds, resulting in the appearance, disappearance, and movement of Raman peaks (Fig. 6f).[127]

Although several advanced characterization techniques have been used to verify the capability of catalysts in producing urea, some limitations still remain for a single strategy.[128] A combination of microscopic, spectroscopic, and other techniques is necessary to clarify the catalyst structure, which is beneficial for obtaining the practical reaction mechanism of the C–N coupling process. In addition, several *in situ* techniques can aid in monitoring and comprehending catalyst changes under specific reaction conditions and their effect on reaction pathways under specific reaction conditions.[129] With

Table 1 Previously reported electrocatalysts for electrocatalytic synthesis of urea based on carbon dioxide as a carbon source and different nitrogen-containing small molecules as a nitrogen source

| Catalyst	Media	C and N sources	Key intermediates	FE%	Detection method	Yield rate	Stability (h)	Configuration	Ref.
Pd₁Cu₁/TiO₂-400	1 M KHCO₃	CO₂, N₂	*NCON*	8.92	Urease method	3.36 mmol g⁻¹ h⁻¹	12	H-cell	Chen et al. (2020)[28]
BiFeO₃/BiVO₄	0.1 M KHCO₃	CO₂, N₂	*NCON*	17	DAMO-TSC	4.94 mmol g⁻¹ h⁻¹	10	H-cell	Yuan et al. (2021)[95]
Bi-BiVO₄	0.1 M KHCO₃	CO₂, N₂	*NCON*	12.55	DAMO-TSC	5.91 mmol g⁻¹ h⁻¹	10	H-cell	Yuan et al. (2021)[94]
CuPc NTs	0.1 M KHCO₃	CO₂, N₂	*NCON*	12.99	DAMO-TSC	2.39 mmol g⁻¹ h⁻¹	10	H-cell	Mukherjee et al. (2022)[143]
Ni(BO₃)₂-150	0.1 M KHCO₃	CO₂, N₂	*NCON*	20	DAMO-TSC	9.70 mmol g⁻¹ h⁻¹	20	H-cell	Yuan et al. (2021)[116]
Vₙ-Cu₃N-300	0.1 M KHCO₃	CO₂, N₂	*NCON*	28.7	DAMO-TSC	2.67 mmol g⁻¹ h⁻¹	10	H-cell	Lv et al. (2023)[144]
V_O-InOOH	0.1 M KNO₃	CO₂, NO₃⁻	*CO₂NO₂	51	DAMO-TSC	9.88 mmol g⁻¹ h⁻¹	10	H-cell	Lv et al. (2022)[85]
Fe-Fe₃O₄/CNs	0.1 M KNO₃	CO₂, NO₃⁻	*CONH₂	16.5	DAMO-TSC	24.2 mmol g⁻¹ h⁻¹	10	H-cell	Geng et al. (2023)[145]
Ru-Cu CF	0.1 M KNO₃	CO₂, NO₃⁻	*CONH₂	25.4	DAMO-TSC	0.00253 mmol cm⁻² h⁻¹	10	H-cell	Qin et al. (2022)[146]
In(OH)₃-S	0.1 M KNO₃	CO₂, NO₃⁻	*CO₂NO₂	53.4	DAMO-TSC	8.89 mmol g⁻¹ h⁻¹	8	H-cell	Lv et al. (2021)[41]
TiO₂/Nafion	0.1 M KNO₃	CO₂, NO₃⁻	*CONH₂	40	Urease method	N/A	5.2	H-cell	Saravanakumar et al. (2017)[136]
Cu/ZnO GDEs	0.1 M KNO₃	CO₂, NO₃⁻	*CONH₂	37.4	DAMO-TSC	16 mmol g⁻¹ h⁻¹	5	Flow cell	Wang et al. (2023)[147]
CuWO₄	0.1 M KNO₃	CO₂, NO₃⁻	*CONO₂	70.1	Urease method	1.64 mmol g⁻¹ h⁻¹	10	H-cell	Zhao et al. (2023)[122]
FeNi₃	0.1 M KNO₃	CO₂, NO₃⁻	N/A	16.58	Urease method	8.23 mmol g⁻¹ h⁻¹	N/A	H-cell	Wang et al. (2023)[55]
Co₁-TiO₂	1 M KNO₃	CO₂, NO₃⁻	*OCNO	36.2	Urease method	212.8 mmol g⁻¹ h⁻¹	N/A	H-cell	Tu et al. (2024)[148]
XC72R-AuPd	0.075 M KHCO₃ + 0.025 M KNO₃	CO₂, NO₃⁻	*CONH₂	15.6	DAMO-TSC	3.4 mmol g⁻¹ h⁻¹	10	H-cell	Wang et al. (2022)[40]
Cu-GS-800	0.1 M KHCO₃ + 0.1 M KNO₃	CO₂, NO₃⁻	*CONH₂	28	DAMO-TSC	30.63 mmol g⁻¹ h⁻¹	N/A	H-cell	Leverett et al. (2022)[65]
F-CNT-300	0.1 M KHCO₃ + 0.1 M KNO₃	CO₂, NO₃⁻	*CONH₂	18	DAMO-TSC	6.36 mmol g⁻¹ h⁻¹	8	H-cell	Liu et al. (2022)[108]
Bi:10%In/C NPs	0.1 M KHCO₃ + 0.1 M KNO₃	CO₂, NO₃⁻	*CONH₂	20.31	Urease method	10.1 mmol g⁻¹ h⁻¹	N/A	H-cell	Mao et al. (2024)[125]
m-Cu₂O	0.1 M KHCO₃ + 10 mM KNO₃	CO₂, NO₃⁻	*OCNO	9.43	Urease method	29.2 mmol g⁻¹ h⁻¹	N/A	H-cell	Wang et al. (2023)[149]
B-FeNi-DASC	0.1 M KHCO₃ + 50 mM KNO₃	CO₂, NO₃⁻	*CONH₂	17.8	Urease method	20.2 mmol g⁻¹ h⁻¹	N/A	H-cell	Zhang et al. (2022)[76]
Cu₁-CeO₂	0.1 M KHCO₃ + 50 mM KNO₃	CO₂, NO₃⁻	*OCNO	N/A	Urease method	52.84 mmol g⁻¹ h⁻¹	4	H-cell	Wei et al. (2023)[66]
Vo-CeO₂-750	0.1 M KHCO₃ + 50 mM KNO₃	CO₂, NO₃⁻	*OCNO	N/A	Urease method	15.7 mmol g⁻¹ h⁻¹	5	H-cell	Wei et al. (2022)[86]
3D Zn/Cu hybrid	0.1 M KHCO₃ + 1000 ppm KNO₃	CO₂, NO₃⁻	*CO₂NO₂	67	DAMO-TSC	55.3 mmol g⁻¹ h⁻¹	32	Flow cell	Luo et al. (2023)[121]
Cu@Zn	0.2 M KHCO₃ + 0.1 M KNO₃	CO₂, NO₃⁻	*CONH₂	9.28	¹H-NMR	0.00729 mmol cm⁻² h⁻¹	12	H-cell	Meng et al. (2022)[151]
CuInS₂/TF	0.05 M KHCO₃ + 0.05 M KNO₃	CO₂, NO₃⁻	*CONH₂	19.6	DAMO-TSC	50.29 mmol g⁻¹ h⁻¹	N/A	H-cell	Chen et al. (2024)[152]
CuO₅₀ZnO₅₀	0.1 M Na₂SO₄ + 0.1 M NaNO₃	CO₂, NO₃⁻	N/A	41	Urease method	N/A	N/A	H-cell	Anastasiadou et al (2023)[153]
Te-doped Pd	0.1 M KHCO₃ + 0.01 M KNO₂	CO₂, NO₂⁻	*CONH₂	12.2	DAMO-TSC	N/A	5	H-cell	Feng et al. (2020)[57]
ZnO-Vo	0.2 M NaHCO₃ + 0.1 M NaNO₂	CO₂, NO₂⁻	*CONH₂	23.3	HPLC	16.56 mmol g⁻¹ h⁻¹	15	H-cell	Meng et al. (2021)[87]
Co-NiOₓ@GDY	0.01 M NaNO₂	CO₂, NO₂⁻	*CONH₂	64.3	DAMO-TSC	15.1 mmol g⁻¹ h⁻¹	N/A	H-cell	Zhang et al. (2022)[98]
Cu-TiO₂-Vo	0.2 M KHCO₃ + 0.02 M KNO₂	CO₂, NO₂⁻	*CONH₂	43.1	Urease method	20.8 mmol g⁻¹ h⁻¹	N/A	H-cell	Cao et al. (2020)[89]
Au-Cu (SANFs)	0.5 M KHCO₃ + 0.01 M KNO₂	CO₂, NO₂⁻	*CONH₂	24.7	DAMO-TSC	64.8 mmol g⁻¹ h⁻¹	N/A	H-cell	Liu et al. (2022)[56]
Zn NBs	0.2 M KHCO₃	CO₂, NO	*CONH₂	11.26	DAMO-TSC	15.13 mmol g⁻¹ h⁻¹	N/A	Flow cell	Huang et al. (2022)[29]
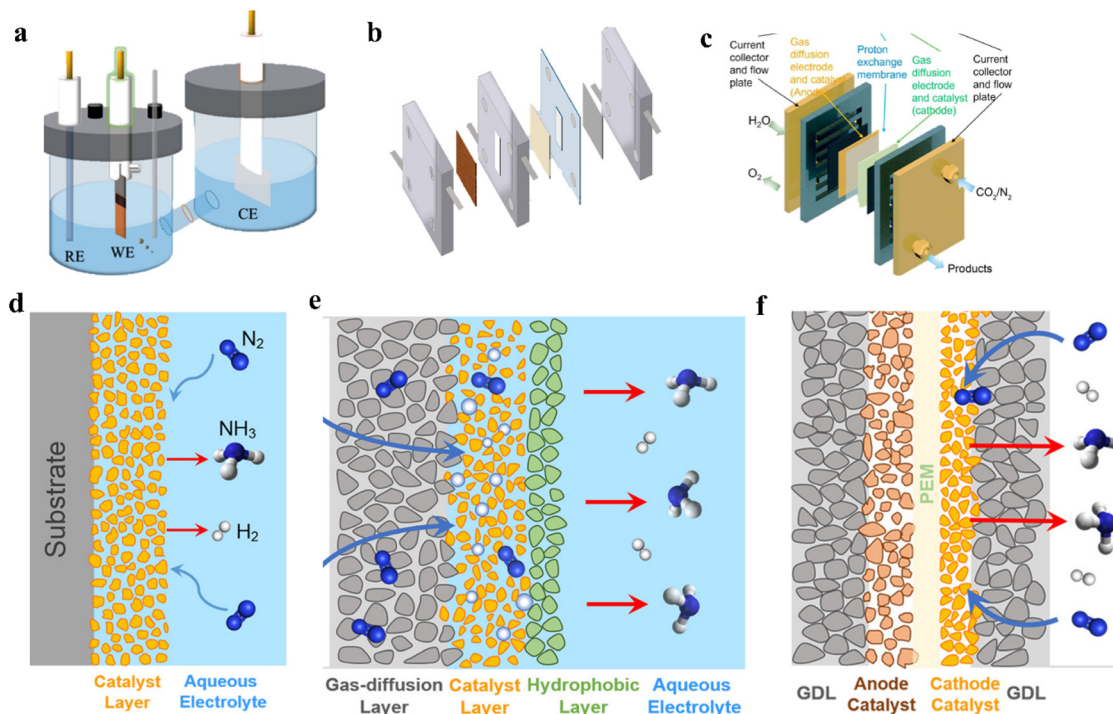
Fig. 7 (a) H-cell for urea synthesis. (b) Flow-cell for urea synthesis. (c) MEA cell for urea synthesis. (d) Schematic illustration of solid−liquid interface in H-cell. (e) Schematic diagram of a membrane-based flow reactor. (f) Schematic illustration of solid−liquid interface in MEA cell. Reproduced from ref. 179, with permission from Royal Society of Chemistry, copyright 2023. (a and b) Reproduced from ref. 180, with permission from American Chemical Society, copyright 2022. (d, e and f) Reproduced from ref. 181, with permission from Royal Society of Chemistry, copyright 2022.

the continuous deepening of mechanism exploration, the more favored urea production process will be revealed. At this point, a suitable reactor with considerable mass transfer and reaction stability ensures an optimal environment for the operation of catalytic systems.

5. Electrochemical cells for urea synthesis

The yield of electrocatalytic urea synthesis is affected by current density, carbon dioxide solubility, and catalytic system stability. The type of electrolyzer affects the current density and the reactant mixing degree, and the stability of the operating system determines the product yield and distribution. Therefore, electrolytic cells play a crucial role in transmuting CO_2 and N-sources to value-added chemical products.[39,130] Generally, the electrolytic cell is composed of two half-reactions: the reduction reaction on the cathode and the oxidation reaction on the anode. By setting an ion exchange membrane between the cathode and anode, ions can transport across the membrane and maintain the charge equilibrium of the whole system. On the other hand, a reference electrode is always added in cells to ensure the accuracy of potentials. To fulfill different experimental requirements, three types of electrochemical reactors are discussed for the electrochemical syn-

thesis of urea, including H-type cells, flow cells, and membrane electrode assembly (MEA) cells.

5.1 H-cell

The H-cell is the most widely used lab-scale electrochemical reactor, where the working and reference electrodes are placed in the cathodic compartment, while the counter electrode is in the anodic compartment. An ion-exchange membrane is used to separate the two compartments and prevent the mixing and re-oxidation of products in different phases. In general, platinum mesh and carbon rod are better candidates to be used as counter electrodes, the working electrode can utilize metal foils or electrocatalyst-loaded glassy carbon/carbon paper, while the reference electrode can be Ag/AgCl electrodes and Hg/Hg_2SO_4 according to the pH value of the operating system (Fig. 7a and d).

During the electrocatalytic synthesis of urea, carbon dioxide (CO_2) is continuously introduced into the cathode compartment to react with the nitrogen source in the electrolyte. The resulting gas products are then analyzed using a gas chromatograph (GC) and the faradaic efficiencies of gas products are determined based on the obtained data. The liquid products in the cathode chamber are collected after the electrolysis and measured using a suitable method (*e.g.*, NMR, spectroscopic method, *etc.*) to determine the urea faradaic efficiency.[40]

However, urea synthesis in the H-cell suffers from the low solubility of CO_2 and N_2 (−34 mM and −0.6 mM, respectively,

under ambient conditions), high resistance to electrochemical reactions, and low scalability of the device, which result in low efficiency.[131] Therefore, finding a way to strengthen the interactions between feedstocks and active sites to improve the efficiency of the reactions has high priority in current research.

5.2 Flow cell reactor

Derived from the fuel cell field, the flow cell can substantially improve the mass transfer efficiency and overcome the mass transfer limitations in H-cells. In flow cells, it is feasible for the low-solubility CO_2 and N_2 to contact active sites through the gas phase, and the products are more easily recycled from the liquid phase. The flow cell has a similar structure to the H-cell, namely an anode compartment, a cathode compartment, and an ion exchange membrane. The cathode is a gas diffusion electrode (GDE), which has a gas diffusion layer (GDL) and a catalytic layer (CL). The GDL is hydrophobic and facilitates the transport of gases and products. It also supports the CL and allows gas to directly reach the cathode surface. The anode always employs a commercialized catalyst-loaded GDE, and the reference electrode can be Ag/AgCl or standard hydrogen electrode, depending on the experimental requirement (Fig. 7b and e). In comparison with the H-cell, lower cell resistance can be achieved in the flow cell, due to the proximity of the anode and cathode.

Similar to the H-cell, the gas path of the flow cell directly connects with a gas chromatograph (GC), enabling cathode gas products from the electrolysis process to be monitored by GC. Wang and coworkers synthesized urea by electrocatalytic coupling of N_2 and CO_2 using Pd_1Cu_1/TiO_2-400 as the catalyst.[28] They found that the flow cell enhanced the urea formation rates compared with the H-cell. The highest rate was 3.36 mmol g^{-1} h^{-1} with a faradaic efficiency of 8.92% at −0.4 V vs. RHE in the flow cell, while the rate was 0.19 mmol g^{-1} h^{-1} with a faradaic efficiency of 1.56% at −0.4 V vs. RHE in the H-cell. However, GDE flooding is a serious problem when employing large overpotentials. In addition, the manufacturing costs of GDE and carbonate by-product formation also restrict the large-scale application of the flow cell.

5.3 Membrane electrode assemblies (MEA)

The MEA cell is a promising design for various electrochemical reduction reactions, since it possesses low ohmic loss and high energy efficiency. A MEA cell has three main components: a proton exchange membrane, a catalytic layer, and a gas diffusion layer.[132,133] The proton exchange membrane conducts protons quickly and prevents the crossover of hydrogen, oxygen, and nitrogen between the cathode and anode. MEA can facilitate ion transportation and serves as a barrier against the crossover of gas and electrons. The gas, ions, and electrons can be gathered at the triple-phase boundary, which is the catalyst surface, to enhance mass transfer efficiency (Fig. 7c and f).

As electrocatalytic urea synthesis is currently limited within laboratory-scale productivity, some key aspects need to be addressed to attain the standards for practical applications.

For example, the yield, current density, and faradaic efficiency correspond to the mass transfer phenomenon. Therefore, reactor design plays a crucial role in eliminating the limitations of electrocatalytic urea synthesis. From the viewpoint of building a reactor, H-cells are simple to build and the products are easy to separate, but it is still difficult to meet the performance requirements owing to the impacts of concentration polarization and gas solubility. Flow cells have a relatively better mass transfer efficiency, while GDE and ion exchange membranes need to be greatly improved to meet the stability and mass transfer requirements for practical applications. MEA reactors can achieve a higher reaction efficiency, but the liquid products in the system are difficult to collect. Based on the above three common reactors, the new design of reactors should be modified accordingly to address the abovementioned concerns. To achieve a long-term electrolyzer for practical applications, the impurities of electrolytes, membrane durability, mass transfer characteristics, and electrothermal effect that causes temperature changes should be comprehensively considered.[134] Particularly, the membrane is the important unit for constructing long-term stabilized electrolyzers. The further improvement of anti-degradation and anti-pollution capabilities will facilitate its practical applications in a complex reaction environment.

6 Urea identification and quantification

Product testing is an important step in electrocatalytic urea synthesis; its accuracy determines the credibility of products. Various methods have been developed for urea identification and quantification, being suitable for different reaction conditions. In order to select an optimal method for urea quantification, the experimental quantification minimum (EQM) and the potential interference of the electrocatalytic system are the key factors that need to be rated.[135] So far, four main detection methods are available for urea testing: the urease method, diacetylmonoxime-thiosemicarbazide method (DAMO-TSC), ^{1}H-NMR method, and high-performance liquid chromatography (HPLC) (Fig. 8g).[28,86,87,136]

6.1 Urease method

The urease method has been a commonly used method for detecting urea since 1995. In the presence of urease, the urea can be decomposed into ammonia and carbon dioxide at the optimal temperature (37 °C, 40 min).[137] The amount of urea can be calculated according to the principle of conservation of nitrogen atoms ($n_{(urea)} = 2 \times n_{(ammonia)}$). Then, indophenol blue method is used in determining the concentration of ammonia at $\lambda = 655$ nm (Fig. 8a).[138] An appropriate dilution is essential for accurate urea quantification, since high concentrations of urea (>7.0 μg ml^{-1}) may deviate from the linear relationship. However, the activity of urease is affected by various factors such as temperature, pH and urea concentration. Particularly, interfering metal ions from electrolyte impurities or catalyst-
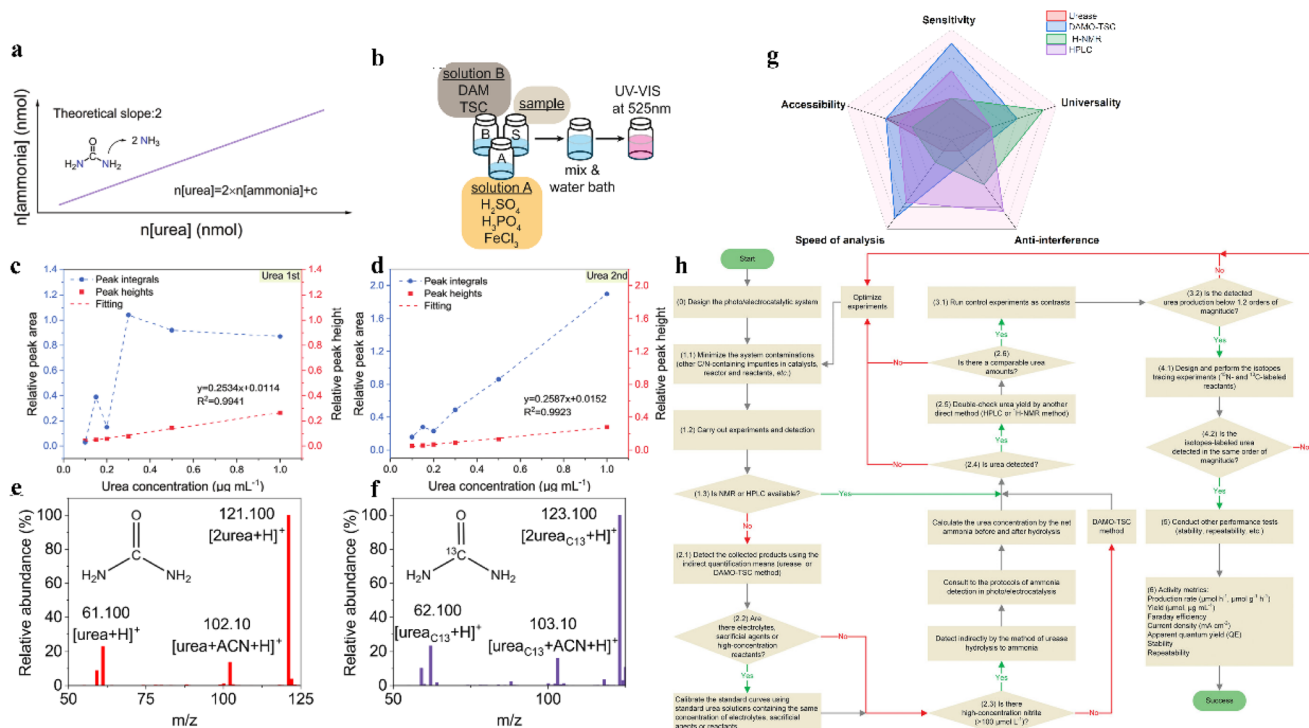
Fig. 8 (a) The conservation principle of nitrogen atoms in the urease method. (b) Illustration of a typical urea colorimetric detection method. (c and d) Urea processed by the methods of peak heights and peak integrals at low-concentration range. Reproduced from ref. 141, with permission from Wiley-VCH, copyright 2023. (e) Mass spectrum of unlabeled (^{12}C) urea in 0.2 M KHCO$_3$. (f) An example of total ion chromatogram (TIC) and extracted ion chromatograms (EIC) for the 10 ppm urea standard. Reproduced from ref. 142, with permission from Elsevier, copyright 2023. (g) The comparison of four detection methods in this study. (h) The proposed photo/electrocatalytic urea synthesis and quantification protocol. Reproduced from ref. 135, with permission from Wiley-VCH, copyright 2022.

leaching metals cannot be ignored. The presence of Ni^{2+}, Cu^{2+}, Zn^{2+}, Fe^{3+}, and In^{3+} ions has a negligible effect on urea detection, while the presence of Co^{2+}, Fe^{2+}, and Mn^{2+} ions will inhibit urease activity, leading to errors in the measurement.[138] The restricted reaction temperature, high cost, and long detection time also limit the operation of the urease method. Meanwhile, the NH$_4^+$ losses during the heating process may also contribute to false reporting. Therefore, adjusting the testing strategy based on the experimental details is important in the application of the urease method.

6.2 Diacetylmonoxime-thiosemicarbazide method (DAMO-TSC)

The DAMO-TSC method is another widely used technique for quantifying urea. It offers several advantages over the traditional urease decomposition method, including faster detection and lower detection limit of urea.

During the detection process, DAMO undergoes hydrolysis under acidic conditions to produce diacetyl. The diacetyl will react with urea to form a yellow-colored diazine product and water. Diazine can be stabilized by thiosemicarbazide and converted into a pink complex with enhanced absorbance in the presence of iron ions, which has a maximum absorption wavelength of 525 nm (Fig. 8b). Furthermore, by adding a specific concentration of antipyrine, thiourea, metal ions, and other

substances, the sensitivity of the reaction between urea and diacetyl can be improved. This addition can also improve the stability of the color development.

It is noted that the effect on color development by interfering substances should be considered before detection. The colorimetric determination is affected by carbon products (such as formic acid and isopropanol), nitrogen products (such as ammonia and hydrazine), and common ionic species (such as metal cations, NO$_2^-$, and NO$_3^-$).[139] Nitrite is the most problematic of these species; when the concentration of NO$_2^-$ reaches 10 mmol L^{-1}, it interferes with color development due to its strong oxidizing properties. In addition, a strongly acidic environment is necessary for color development. For most electrocatalytic urea synthesis processes, the buffering effect of KHCO$_3$ electrolyte has a minimal tendency of pH shift to alkaline conditions. However, in higher concentrations KOH electrolytes (>1 M), the pH value of collected electrolytes should be adjusted to the optimal range before the quantification.

6.3 ^{1}H-NMR method

The ^{1}H-NMR method is commended by its simplicity, accuracy, and specificity, and the measurements are based on the instrument selection and parameter settings.[29,140] The quantification of urea by ^{1}H-NMR is minimally affected by changing the chemical environment of hydrogen atom-influenced pro-
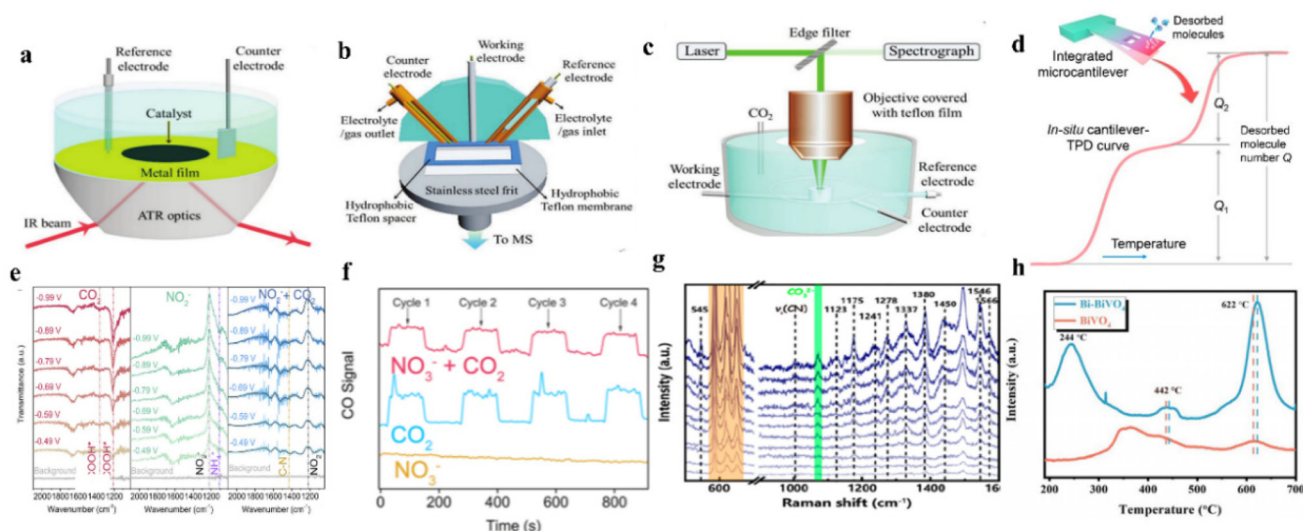
Fig. 9 (a) Schematic of ATR-IR configurations. (b) Schematic of DEMS cell. (c) Schematic of *operando* Raman configurations. (d) Schematic of TPD. Reproduced from ref. 183, with permission from American Chemical Society, copyright 2023. (e) *In situ* ART-IR spectra of ZnO-V under CO_2, $NaNO_2$, and CO_2 with $NaNO_2$. Reproduced from ref. 182, with permission from Elsevier, copyright 2021. (f) Online DEMS spectra of CO signals over Cu@Zn. Reproduced from ref. 151, with permission from American Chemical Society, copyright 2022. (g) Operando electrocatalytic Raman spectra of Ru–Cu CF collected at −0.3 V *vs.* Ag/AgCl. Reproduced from ref. 146, with permission from American Chemical Society, copyright 2022. (h) (CO_2-TPD) plots for $BiVO_4$ and Bi-$BiVO_4$. Reproduced from ref. 94, with permission from Wiley-VCH, copyright 2021. (a, b and c) Reproduced from ref. 154, with permission from Wiley-VCH, copyright 2021.

ducts and metal ions. Noteworthily, most product solutions from the electrocatalytic C–N coupling process involve huge amounts of water molecules, and the water suppression may induce baseline distortions and affect the accuracy of quantification. To avoid these disadvantages, the relative intensities can be calculated by peak integral and peak height methods. The increased variability of multiple assays is due to the proximity of the chemical shift of urea to the water peak and its increased sensitivity to interference from this peak. Therefore, the peak height method can be used to attenuate the effect of water peaks (Fig. 8c and d).[141]

6.4 Liquid chromatography-mass spectrometry (LC-MS)

LC-MS is another method for urea quantification.[87] This method simultaneously possesses the excellent separation capability of liquid chromatography with the high sensitivity and selectivity detection capability of mass spectrometry (Fig. 8e and f).[142] According to the differentiated chemical composition and physical properties of individual components, products can be separated by the liquid chromatography method. The peak intensity is positively correlated to the concentration of separate products. After solvent evaporation at the interface of the LC and MS module, product ionization will occur through electrospray ionization (ESI) or atmospheric pressure chemical ionization (APCI) method. Next, ions are separated based on their charge-to-mass (m/z) ratio in the electric field.

Generally, the urease method is poorly reproducible and susceptible to environmental interference. It is not suitable in the presence of low urea concentrations with high NH_4^+ back-

grounds. The DAMO quantification method is suitable for most systems, but not for environments with high levels of NO_2^- (>10 mmol L^{-1}). The ^{1}H-NMR method is highly resistant to interference, but is strongly influenced by urea concentration, namely, experimental quantification minima are large and few studies have used the LC-MS method to quantify urea. Additionally, the environmental conditions and operating conditions should be strictly controlled during product testing to improve the accuracy, reliability, and anti-interference ability (Fig. 8h). To improve the efficiency and accuracy of product testing, a combination of two or more detection methods is usually required.

7 Mechanism of urea synthesis process

Current studies indicate that the intermediates are critical for a coupling process. However, the exact roles played by these intermediates are still not clear. Therefore, revealing the reaction mechanism and the formation of the intermediates sheds light on enhancing the efficiency of the electrocatalytic systems.[154] To date, the mechanism of the urea synthesis process during electrocatalytic urea synthesis has been investigated by temperature-programmed desorption measurements (TPD) and extensive *in situ* spectroscopy characterization methods, including the *in situ* Fourier transform infrared spectroscopy (*in situ* FTIR), online differential electrochemical mass spectrometry (DEMS), and operand Raman spectroscopy.
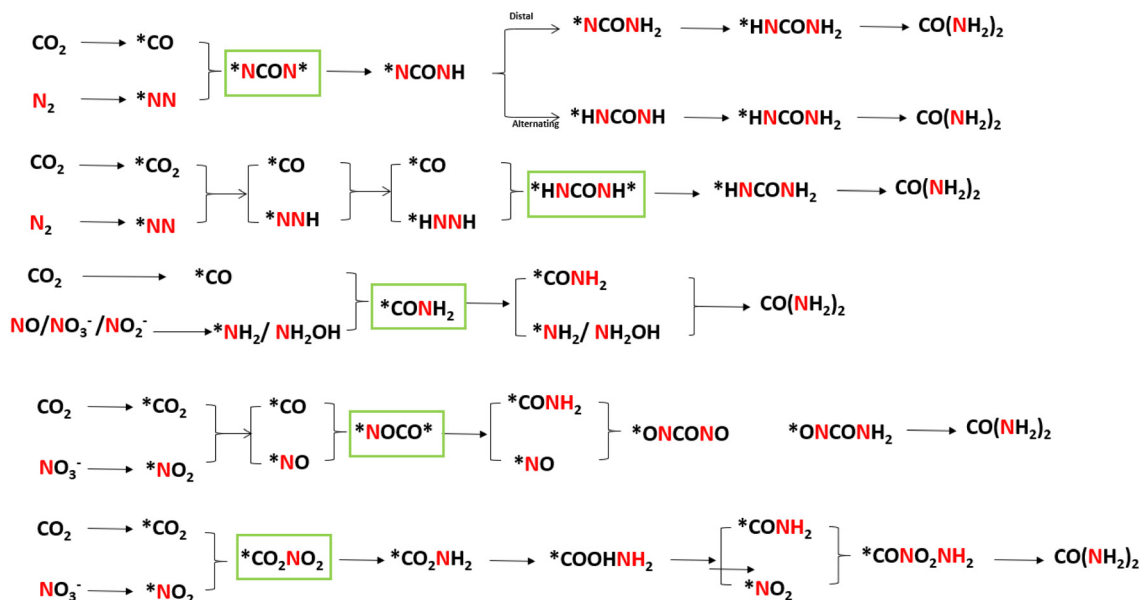
Fig. 10 Reaction pathways for the synthesis of urea by C–N coupling and its intermediates.
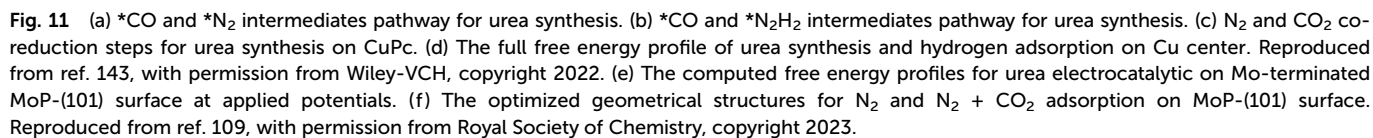
7.1 Determination of intermediates

7.1.1 *In situ* Fourier transform infrared spectroscopy measurements.

The infrared spectrum is widely used to investigate the "fingerprint of molecules". It allows the determination of the spatial configuration and bond length of the target molecule (Fig. 9a).[155] In electrocatalytic urea synthesis, *in situ* FTIR is a powerful tool for analyzing the generation and transformation process of C/N intermediates. Based on the appearance, enhancement, disappearance, or displacement of intermediates on the spectra, the possible reaction pathways can be revealed. In an application scenario, on a ZnO-V catalyst, the characteristic peak of COOH* strengthens gradually at 1360 cm^{-1} and 1210 cm^{-1} when using CO_2 as the feedstock, while the NH_3 signal at 1100 cm^{-1} showed a similar trend by using KNO_2 electrolyte (Fig. 9e).[87] Interestingly, when using CO_2 and KNO_2 as feedstocks, the C–N bond at 1440 cm^{-1} is observed. Meanwhile, the characteristic peak of COOH* disappeared in the spectrum, which suggests COOH* is consumed during urea generation. According to data analysis, the authors deduced a possible reaction pathway for urea formation: an oxygen atom in NO_2^- fills the oxygen vacancy on the surface of ZnO-V and undergoes a multi-step proton-coupled electron transfer process to form the NH_2^* intermediate. After a one-step nucleophilic reaction, COOH* is consumed by the attack of NH_2^* and forms a C–N bond. These distinctive variations make *in situ* FTIR measurements an efficient way to trace the pathway of the C–N coupling process.

7.1.2 Online differential electrochemical mass spectrometry.

The DEMS method combines an electrochemical reaction cell with a mass spectrometer (MS). The cell has a non-wetting porous electrode, which is connected to a porous membrane that leads to the ionization chamber of the MS. It can detect the gases and volatile intermediates consumed or produced at the electrochemical reaction interface in real time (Fig. 9b).[156,157] As another useful tool to reveal the presence/disappearance of the intermediates during the electrocatalytic processes, DEMS spectroscopy is promising for parsing the pathway of urea synthesis (Fig. 9f).[158,159] Also, the online DEMS spectroscopy can reveal the relationship between independent reactions in the system, which makes the entire reaction process more explicit.

7.1.3 *Operando* Raman spectroscopy.

Raman spectroscopy can characterize the rotational, vibrational, and other low-frequency modes of a sample based on its high selectivity and availability.[159] With great potential for detecting surface changes of catalysts (especially metal oxides), the combination of operational Raman spectroscopy and electrochemistry is popular for analyzing the mechanism of electrocatalysis (Fig. 9c). Like the *in situ* FTIR, *operando* Raman spectroscopy can provide valuable information about reaction intermediates. For example, Qin and coworkers clarified the reaction pathway using of Ru–Cu CF as a catalyst, which delivers a high urea yield of $151.6 \text{ μg h}^{-1} \text{ cm}^{-2}$ and a high FE of 25.4% at a low onset potential of 0.13 V *vs.* RHE.[146] They noted that the vibration band at 545 cm^{-1} showed increased intensity in the Raman spectra due to the evolution of the $\delta(\text{NCN})$ and $\delta(\text{NCO})$ bending vibrations in the nucleation process of urea, which indicate the C–N coupling (Fig. 9g).

7.1.4 Temperature-programmed desorption measurements.

TPD test is a dynamic analytical process in which a specific amount of adsorbent adheres to the catalyst surface and is then heated at a controlled rate with inert gas (Fig. 9d).[160] Changes in the composition and concentration of the effluent gas can be detected. Subsequently, the adsorption centers, the active composition, and the reduction properties

Fig. 11 (a) *CO and *N$_2$ intermediates pathway for urea synthesis. (b) *CO and *N$_2$H$_2$ intermediates pathway for urea synthesis. (c) N$_2$ and CO$_2$ co-reduction steps for urea synthesis on CuPc. (d) The full free energy profile of urea synthesis and hydrogen adsorption on Cu center. Reproduced from ref. 143, with permission from Wiley-VCH, copyright 2022. (e) The computed free energy profiles for urea electrocatalytic on Mo-terminated MoP-(101) surface at applied potentials. (f) The optimized geometrical structures for N$_2$ and N$_2$ + CO$_2$ adsorption on MoP-(101) surface. Reproduced from ref. 109, with permission from Royal Society of Chemistry, copyright 2023.

of the catalyst can be evaluated. TPD is frequently employed when N$_2$ is used as a nitrogen source for urea synthesis. For instance, TPD can report the adsorption sequence of N$_2$ and CO$_2$ on Bi-BiVO$_4$ hybrids.[94] The TPD results show that the N$_2$ peak appears at a higher temperature compared with CO$_2$, suggesting that nitrogen is more likely to be adsorbed onto the catalyst surface (Fig. 9h).

In situ analyses provide solutions to monitor the generation of intermediates, bond formation, and reaction dynamics, which can provide new insights for catalyst optimization. However, *in situ* analyses can only detect a few key intermediate reactions, making it difficult to provide a full picture of the complex reaction system. Further exploration is needed to understand the reaction mechanism of electrochemical urea synthesis by using *in situ* measurements. Therefore, characterization such as *in situ* spectroscopic techniques (especially syn-

chrotron radiation-Fourier transform infrared spectroscopy) and theoretical calculations will maintain their popularity in catalytic urea synthesis research.

7.2 Key intermediates in electrocatalytic urea synthesis

Generally, catalysts with the ability to simultaneously catalyze both CO$_2$RR and NRR are more likely to carry out urea electrocatalytic production. With employing differentiated catalysts, the corresponding mechanism and pathways will be changed owing to the production of different C/N intermediates. In recent studies, theoretical calculations (density functional theory and *ab initio* molecular dynamics) have been used to uncover the formation steps of C–N bond. To make the internal relationship easier to understand, we have summarized the formation pathways of different intermediates with C–N bonds in this section, also displayed in Fig. 10.
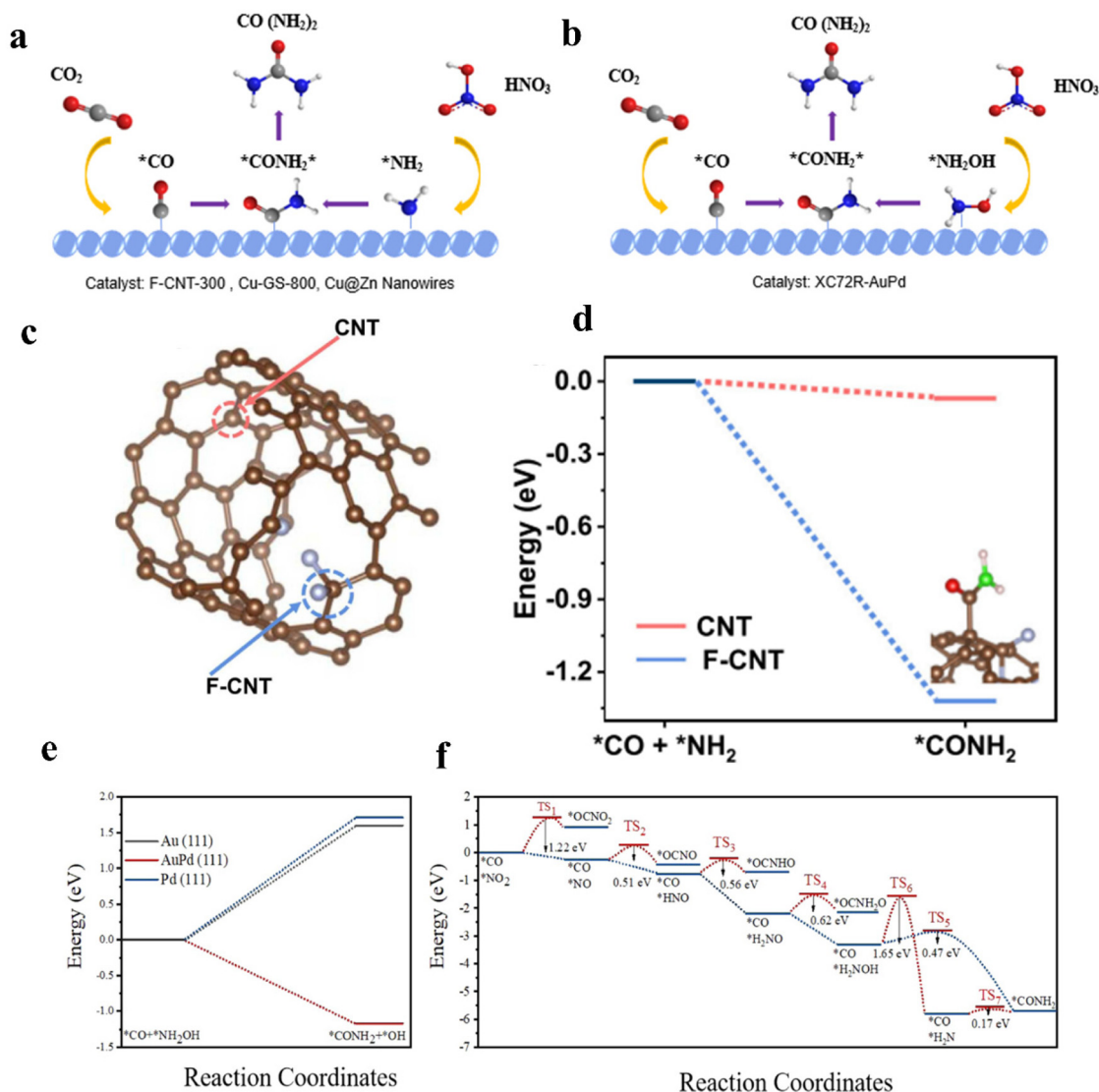
Fig. 12 (a) *CO and *NH$_2$ intermediates pathway for urea synthesis. (b) *CO and *NH$_2$OH intermediates pathway for urea synthesis. (c) CNT structural model in DFT calculations. (d) C–N coupling on CNT and F-doped CNT active sites. Reproduced from ref. 108, with permission from Springer Nature, copyright 2022. (e) Free energies for *CO + *NH$_2$OH → *CONH$_2$ on Au, AuPd, and Pd. (f) The C–N coupling pathway on AuPd. Reproduced from ref. 40, with permission from Elsevier, copyright 2022.

7.2.1 *NCON* and *NHCOHN*. When using N$_2$ as the nitrogen source, the key intermediate of the reaction is *NCON*. Specifically, once the CO is released from the CO$_2$ reduction process, the *N≡N* shows a strong attraction to the CO due to the matched molecular orbitals. The tower-like urea precursor *NCON* is formed after CO binding with *N≡N* (Fig. 11a).[28] Jit Mukherjee and coworker synthesized copper phthalocyanine nanotubes (CuPc NTs) with multiple active sites, and predicted that the rate-determining step is CO* + *NN* → *NCON*.[143] The *NCON* would be further hydrogenated to urea molecules (Fig. 11c and d). Another key intermediate is *NHCOHN*, which originated from the electrocatalytic process by using MoP-(101) (Fig. 11b).[109] Theoretical calculation results showed that *N$_2$H reacts with *CO and is more favorable in kinetics and thermodynamics (Fig. 11e and f).

Subsequently, the *NHCOHN* intermediate can be formed by the combination of hydrogenated *N$_2$H$_2$ with *CO.

7.2.2 *CONH$_2$ and *CONH. In the case of the reaction system from co-reduction of NO/NO$_2^-$/NO$_3^-$ and CO$_2$, *CONH$_2$ is one of the identified intermediates in the C–N coupling process (Fig. 12a). The critical step for F-doped CNT is the *CONH$_2$ formation by coupling *CO with *NH$_2$ (Fig. 12c and d).[108] On the other hand, the *CONH$_2$ can be synthesized on XC72R-AuPd through the combination of *CO and *NH$_2$OH (Fig. 12e and f).[40] In addition, Liu and coworkers used *ab initio* molecular dynamics simulations (AIMD) to investigate the reaction pathway of urea generation on the surface of Cu (100) in neutral solutions.[25] They pointed out that urea was generated through the formation of *CONH intermediate (Fig. 12b). They summarized the reaction potential barrier
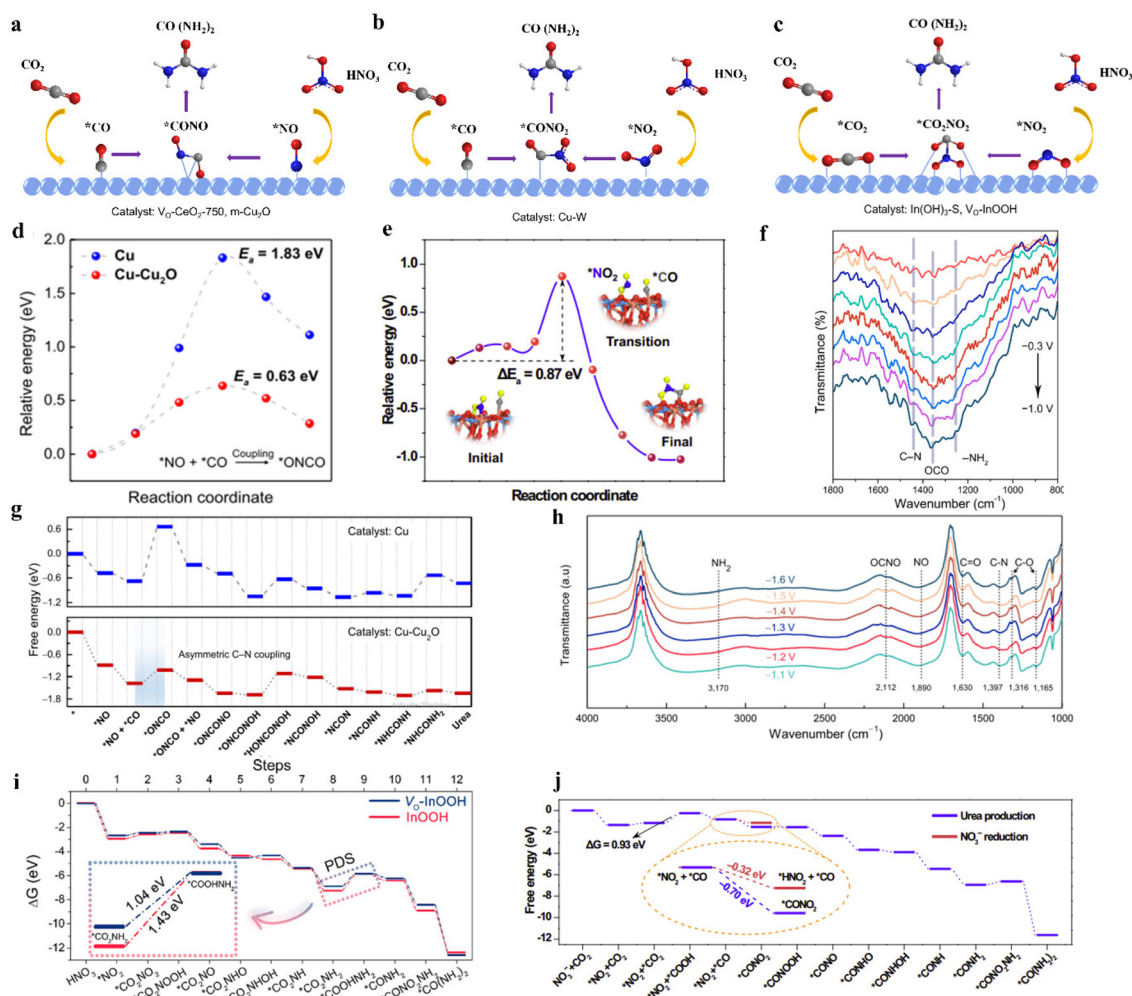
Fig. 13 (a) *CO and *NO intermediates pathway for urea synthesis. (b) *CO and *NO$_2$ intermediates pathway for urea synthesis. (c) *CO$_2$ and *NO$_2$ intermediates pathway for urea synthesis. (d) Urea formation mechanisms and corresponding free energy diagrams along the urea formation pathway on Cu and Cu-Cu$_2$O surfaces. (e) The initial, transition, and final states during the *CONO$_2$ formation are presented. (f) *Operando* SR-FTIR spectra of V$_O$-InOOH at various potentials (−0.3 to −1.0 V *vs.* RHE) in the range of 800–1800 cm^{-1}. (g) The illustration of urea formation mechanisms and corresponding free energy diagrams along the urea formation pathway on Cu and Cu-Cu$_2$O surfaces. (h) Infrared signal in the range of 1000–4000 cm^{-1} under various potentials for m-Cu$_2$O during the electrocoupling of NO$_3^-$ and CO$_2$. Reproduced from ref. 149, with permission from Chinese Chemical Society, copyright 2023. (i) Free-energy diagrams for urea production on the (110) facets of V$_O$-InOOH and pristine InOOH at 0 V *vs.* RHE. Reproduced from ref. 85, with permission from American Chemical Society, copyright 2022. (j) Free-energy diagram for urea production and NO$_3^-$ reduction on the CuWO$_4$. Reproduced from ref. 122, with permission from Springer Nature, copyright 2023.

values of the different intermediates and further concluded that *NOH and *NH, C–N coupling was easier than protonation reactions. Meanwhile, *N–CO and *NH–CO were difficult to hydrogenate at this potential value due to the large reaction potential barrier, which made *NH couple with *NH–CO to form *NH–CO–NH, followed by a protonation reaction to produce urea.

7.2.3   *OCNO. The *OCNO is also a key intermediate in electrocatalytic urea synthesis (Fig. 13a). It was found that the *NO intermediate can be adsorbed onto the V$_O$ sites of the catalyst. On the V$_O$ sites, the subsequent coupling process between *NO with *CO is more favorable than the hydrogenation reaction, and C–N coupling is thermodynamically and kinetically favorable. In addition, the m-Cu$_2$O catalyst exhibits

remarkable applicability for electrochemical urea synthesis activity, including the high urea yield rate of 29.2 mmol h^{-1}g^{-1} and corresponding FE of 9.43% at −1.3 V *vs.* RHE. The authors indicated that CO$_2$ and NO$_3^-$ were reduced to form *CO and *NO, respectively.[149] Then, the asymmetric coupling between the *in situ*-formed *CO and *NO finally induced the generation of *ONCO and the urea products (Fig. 13d, g and h). DFT calculation also confirmed that the coupling of *CO and *NO was thermodynamically and kinetically favored by the rationally designed Cu^0-Cu$^+$site, and finally boosted the urea production.

7.2.4   *CO NO$_2$ and *CO$_2$ NO$_2$. The formation of C–N bonds is typically completed through the nucleophilic attack by nucleophilic nitrogen intermediates. In some specific scenarios, the C–N coupling can also be facilitated by chemical

steps that do not require a nucleophile attack (Fig. 13b and c). $CuWO_4$ catalyst with the native bimetallic site can achieve remarkable urea faradaic efficiency of 70.1% at −0.2 V *vs.* RHE.[122] On the active sites of $CuWO_4$, the formation of $*CONO_2$ is the rate-determining step. The coupling of $*NO_2$ and $*CO$ reduces the possibility of desorption of intermediates from complex elementary reactions before C–N formation, which inhibits other side reactions (Fig. 13e and j). Additionally, the V_O-In(OOH) catalyst can produce urea by forming $*CO_2$ and $*NO_2$ during the electrocatalytic process. The direct C–N coupling at an early stage of the reaction signature by inhibiting the formation of by-products thus also enhances the urea yield. DFT calculation illustrates that the surface of the V_O-In(OOH) is fully covered by $*NO_2$, which leads to the inhibition of CO_2 reduction (Fig. 13f and i). On the In atoms, the catalyst enables C–N coupling to form the $*CO_2NO_2$ intermediate. After $*CO_2NO_2$ intermediate is formed, this compound undergoes continuous protonation, and urea can thus be synthesized in the proposed system.

In line with the experimental and theoretical results, a better catalyst should have moderate hydrogen adsorption strength to accomplish the intermediates' hydrogenation rather than a strong hydrogen evolution. Meanwhile, a strong oxygen adsorption may induce the feedstocks and oxygenated intermediates to adsorb on the reactive sites, which dominate the direction of reactions. On the other hand, the energy barrier is an important determinant of the reaction. The low energy barrier of the C–N coupling step is more beneficial for the generation of urea and other organonitrogens. This is another determining fact that influences the effectiveness of urea production in the existing studies.

8 Summary and outlooks

Electrochemical C–N coupling presents a viable approach for the environmentally friendly and sustainable synthesis of high-value urea under mild conditions. This review aims to provide a deeper understanding of C–N coupling synthesis technology by reviewing catalyst design, characterization, electrolytic cell types, urea quantifications, and mechanistic investigations. We summarize various strategies for catalyst design, including atomic-scale modulation, vacancy engineering, heteroatom doping, alloying, crystal surface modulation, and heterostructure modification. Furthermore, the advantages and shortcomings of H-cells, flow cells, and MEAs are also concluded. Additionally, this review encapsulates four prevalent techniques for urea detection, outlining their respective application contexts.

8.1 Develop superior electrocatalysts

The development of high-quality electrocatalysts with high activity and selectivity is crucial in electrocatalytic urea synthesis.[161] Several factors are important in designing efficient catalysts: firstly, the ability to adsorb and activate CO_2 and nitrogenous species. On catalysts, the physical adsorption of CO_2 is more favorable than the chemical adsorption. For instance, Mo, Co, Rh, and Ir exhibit a more stable chemisorption of CO_2, rendering them unsuitable as catalysts for urea production, while Zn, Cd, and In display a stronger physical adsorption capacity of CO_2 and have been identified to possess superior ability in urea production.[162,163] Additionally, the catalyst should also have sufficient active sites to enable the simultaneous reduction of various reactants. The efficiency of a catalyst can be maximized by adjusting the density of active sites on its surface, which can be achieved by alloying, defect formation, coordination, and doping methods. The modification of electrocatalysts with multiple active centers is crucial for the simultaneous reduction of carbon and nitrogen-containing species. Lastly, the stability of catalysts plays the key role in determining the feasibility of scaled-up urea synthesis. Catalyst poisoning, aggregation, sintering and dissolution always lead to the inactivation of electrocatalysts during the electrocatalytic process. From the perspective of catalyst design, a catalyst carrier with high specific surface area, chemical stability and thermal stability is beneficial for improving the stability and reactivity of proposed electrocatalysts. Meanwhile, surface modification can effectively optimize the electronic structure of electrocatalysts, which can lead to an adjustment of adsorption properties of intermediates and minimize the production of unwanted byproducts (especially CO).[164]

8.2 Control the reaction environment

Generally, urea synthesis from carbon dioxide and nitrogenous molecules co-reduction occurs predominantly at the region of the reaction interface between the liquid electrolyte, the gaseous reactants, and the solid electrocatalysts. In this reaction environment, electrocatalyst-level, electrolyte-level, and electrochemical cells should be carefully considered. Improving the affinity of catalysts to reactants and enhancing their hydrophobicity could potentially stabilize key intermediates. The anode ions (such as OH^-, HCO_3^-, CO_3^{2-}, or NO_3^-) and the cathode ions (such as OH^-, HCO_3^-, CO_3^{2-}, or NO_3^-) have a significant impact on the local pH value, electrochemical double layer, and distribution of the electric field.[150,165,166] The structure of the device influences the flow rates of mass and the pressures within the gas and liquid phases, thereby governing the stability and selectivity of the coupling reaction products.

8.3 Inhibit side reactions

Side reactions lower faradaic efficiency and may affect product separation. Any irrelevant hydrogenation reactions like CO_2RR, NRR, and HER should be suppressed. Meanwhile, the C–N coupling reaction should always be confined to a narrow potential window since the C/N-intermediates tend to form C–N bonds in the low overpotential region. The urea synthesis reaction requires the coupling of preferred C-intermediates/N-intermediate pairs, such as $*CO/*NH_2$, $*COOH/*NH_2$, and $*CO_2/*NO_2$. In addition, the over-hydrogenation of C/N sources will inhibit the necessary C–N coupling process. Moreover, the

HER can have a significant impact on the formation of C/N intermediates, which will interfere with the operation of the entire system by impeding the electron transfer during urea synthesis.[167]

8.3.1 Inhibition of by-product formation from C and N-intermediates. CO and NH_3 are the main by-products in the C–N coupling reactions.[168] To minimize the production of unexpected CO, it is crucial to enhance the adsorption energy between *CO and active sites, thus facilitating the C–N coupling steps. However, caution should be taken to avoid the over-strong *CO adsorption binding capacity, since it will result in catalyst poisoning, thus impeding subsequent related reactions. Therefore, a suitable *CO binding energy is vital to inhibit by-products and optimize the efficiency of the C–N coupling process. For the adsorbing *CO intermediates on the catalyst, it is possible to accept N intermediates from the adjacent free state and catalytic site, while transferring *CO to the adjacent active sites to accomplish the C–N coupling reaction. Hence, the active sites play a crucial role in the C–N coupling process. On the other hand, over-hydrogenation of N-intermediates also brings serious implications to the C–N coupling reaction. Once N-species are hydrogenated to NH_3, the production efficiency of urea will be extremely inhibited. It is thus vital to prevent any further hydrogenation of N-intermediates that leads to NH_3 formation.

8.3.2 Inhibition of HER. In aqueous reactions, HER has always been carried out with target reactions due to the proximity of their potential window, which will significantly reduce the product yield.[88,169] HER usually happens by the Volmer–Heyrosky and Volmer–Tafel pathways.[170] The adsorbed hydrated protons (H_3O) are reduced to produce H* (intermediate) *via* a Volmer step. In the Heyrosky route, the adsorbed H* combines with the hydrated proton to form H_2. In addition, two H* combine to form H_2 through the Tafel route. To suppress the HER, increasing the pH of the electrolyte to decrease the proton concentration and the use of single-atom catalysts are feasible ways. Moreover, surface modification of the catalysts is another efficient way to suppress the HER by adjusting related energy barriers and binding energy.

8.4 Challenges for industrialized applications

To evaluate the potential for industrializing C–N coupled urea technology, a thorough techno-economic analysis (TEA) is necessary. This analysis should determine the costs of an electrochemical urea synthesis strategy, including feedstock costs, energy costs, and operation costs. In operation costs, the byproduct separation cost holds an important position in determining the comprehensive costs. The side production is a key factor affecting the feasibility of scaled-up urea electrosynthesis. A complicated product separation process is needed when various products including urea, nitrite, ammonia, and other organonitrogen products are produced in the C–N coupling system. In contrast, to develop efficient separation methods, a high-performance urea synthesis method is more suitable to reduce separation costs. Despite the increasing maturity of electrocatalytic urea synthesis technology, the

electrochemical process must achieve a Faraday efficiency of at least 73.24% at a given electricity price of 0.03 kW h^{-1} to be competitive with current urea production.[171] Therefore, it is critical to develop catalysts with excellent product yield and selectivity at industrial-scale current densities (>100 mA cm^{-2}). It is necessary to recognize that the current density, Faraday efficiency, and yield are not solely influenced by the electrocatalyst but also by the architecture of the electrochemical reactor. The structure of the electrode has a direct implication on charge transfer, gas conversion, and mass diffusion, which can significantly affect reaction kinetics. An ideal electrocatalytic reactor should effectively facilitate electron transfer, ion transport, and controlled gas diffusion while preventing the mixing of anode and cathode electrolytes.

With the maturity of electrocatalytic technology, energy sources will be the last issue to hinder large-scale application of electrosynthesis. The revolution of renewable energy is becoming essential to solve the release of greenhouse gases and fossil fuel shortages in future decades.[172,173] Among the current candidates, solar-fueled photovoltaic technology is one of the most promising energy sources around the world. On the technological basis of silicon and thin-film solar cells, the photoconversion efficiencies of dye-sensitized, perovskite, organic, and quantum dot-sensitized solar cells are greatly improved.[174] Particularly, the greatly developed perovskite tandem solar cell provides an opportunity to further improve the photoconversion efficiency.[175,176] With the optimization of solar cell stability and operating costs, photovoltaic power supply facilities could be a strategy option for the synthesis of green urea.

8.5 Machine learning in assisting electrocatalytic urea synthesis

Electrocatalytic synthesis of urea necessitates the formation of C–N bonds, requiring catalysts that concurrently facilitate carbon dioxide reduction and nitrogen reduction reactions. However, during the urea formation process, the desorption of the intermediate *CO and further hydrogenation of *NH_2 can lead to the formation of CO and NH_3 by-products, interfering with the reaction. Therefore, appropriate binding energies for intermediates are also crucial. Nevertheless, traditional methods of synthesizing electrocatalysts are complex and time-consuming, which often results in a long trial-and-error process to successfully design an effective catalyst. Machine learning (ML) techniques, particularly deep learning and reinforcement learning, can be employed to predict and optimize the performance of new catalysts, addressing the bottlenecks in electrocatalytic urea synthesis.[177,178] By selecting suitable descriptors and algorithms to build ML models, we can rapidly screen for catalysts rich in active sites, capable of both CO_2RR and NRR, and where reaction intermediates can timely couple at active sites to form C–N bonds while suppressing the HER. With the development of "big data" and mechanistic investigation, we believe that novel designed catalysts will be increasingly applicable for developing sustainable and economically friendly urea synthesis.

Conflicts of interest

There are no conflicts to declare.

Acknowledgements

References

1 T. Kim and G. T. R. Palmore, *Nat. Commun.*, 2020, **11**, 3622.

2 S. Möhle, M. Zirbes, E. Rodrigo, T. Gieshoff, A. Wiebe and S. R. Waldvogel, *Angew. Chem., Int. Ed.*, 2018, **57**, 6018–6041.

3 T. Tang, Z. Wang and J. Guan, *Coord. Chem. Rev.*, 2023, **492**, 215288.

4 T. Tang, Z. Wang and J. Guan, *Exploration*, 2023, **3**, 20230011.

5 W. Wang, C. Zeng and N. Tsubaki, *Green Carbon*, 2023, **1**, 133–145.

6 G. A. Olah, G. K. S. Prakash and A. Goeppert, *J. Am. Chem. Soc.*, 2011, **133**, 12881–12898.

7 W. Zhu, R. Michalsky, Ö. Metin, H. Lv, S. Guo, C. J. Wright, X. Sun, A. A. Peterson and S. Sun, *J. Am. Chem. Soc.*, 2013, **135**, 16833–16836.

8 X. Li, Y. Chen, X. Zhan, Y. Xu, L. Hao, L. Xu, X. Li, M. Umer, X. Tan, B. Han, A. W. Robertson and Z. Sun, *Innov. Mater.*, 2023, **1**, 100014.

9 X. Wang, B. Liu, Y. Zhang, T. Butburee, K. Ostrikov, S. Wang and W. Huang, *EcoEnergy*, 2023, **1**, 108–153.

10 W. Zhu, Y.-J. Zhang, H. Zhang, H. Lv, Q. Li, R. Michalsky, A. A. Peterson and S. Sun, *J. Am. Chem. Soc.*, 2014, **136**, 16132–16135.

11 A. R. Woldu, Z. Huang, P. Zhao, L. Hu and D. Astruc, *Coord. Chem. Rev.*, 2022, **454**, 214340.

12 D. Yang, Q. Zhu and B. Han, *Innovation*, 2020, **1**, 100016.

13 P. Zhu and H. Wang, *Nat. Catal.*, 2021, **4**, 943–951.

14 W. Luc, X. Fu, J. Shi, J.-J. Lv, M. Jouny, B. H. Ko, Y. Xu, Q. Tu, X. Hu, J. Wu, Q. Yue, Y. Liu, F. Jiao and Y. Kang, *Nat. Catal.*, 2019, **2**, 423–430.

15 S. Verma, S. Lu and P. J. A. Kenis, *Nat. Energy*, 2019, **4**, 466–474.

16 S. Akkari, V. Vivier and C. M. Sánchez-Sánchez, *Electrochim. Acta*, 2024, **474**, 143526.

17 Y. Manaka, Y. Nagatsuka and K. Motokura, *Sci. Rep.*, 2020, **10**, 2834.

18 S. Giddey, S. P. S. Badwal and A. Kulkarni, *Int. J. Hydrogen Energy*, 2013, **38**, 14576–14594.

19 S. M. Lemkowitz, J. C. Van Erp, D. M. Rekers and P. J. Van Den Berg, *J. Chem. Technol. Biotechnol.*, 1980, **30**, 85–101.

20 M. Pérez-Fortes, A. Bocin-Dumitriu and E. Tzimas, *Energy Procedia*, 2014, **63**, 7968–7975.

21 F. Barzagli, F. Mani and M. Peruzzini, *Green Chem.*, 2011, **13**, 1267–1274.

22 J. Zhang, C. D. Sewell, H. Huang and Z. Lin, *Adv. Energy Mater.*, 2021, **11**, 2102767.

23 J. Wang, Y. Gao, H. Kong, J. Kim, S. Choi, F. Ciucci, Y. Hao, S. Yang, Z. Shao and J. Lim, *Chem. Soc. Rev.*, 2020, **49**, 9154–9196.

24 J. Li, Y. Zhang, K. Kuruvinashetti and N. Kornienko, *Nat. Rev. Chem.*, 2022, **6**, 303–319.

25 X. Liu, Y. Jiao, Y. Zheng, M. Jaroniec and S.-Z. Qiao, *Nat. Commun.*, 2022, **13**, 5471.

26 M. Shibata, K. Yoshida and N. Furuya, *J. Electroanal. Chem.*, 1995, **387**, 143–145.

27 D. B. Kayan and F. Köleli, *Appl. Catal., B*, 2016, **181**, 88–93.

28 C. Chen, X. Zhu, X. Wen, Y. Zhou, L. Zhou, H. Li, L. Tao, Q. Li, S. Du, T. Liu, D. Yan, C. Xie, Y. Zou, Y. Wang, R. Chen, J. Huo, Y. Li, J. Cheng, H. Su, X. Zhao, W. Cheng, Q. Liu, H. Lin, J. Luo, J. Chen, M. Dong, K. Cheng, C. Li and S. Wang, *Nat. Chem.*, 2020, **12**, 717–724.

29 Y. Huang, R. Yang, C. Wang, N. Meng, Y. Shi, Y. Yu and B. Zhang, *ACS Energy Lett.*, 2022, 7, 284–291.

30 A. S. Dutton, J. M. Fukuto and K. N. Houk, *Inorg. Chem.*, 2005, **44**, 4024–4028.

31 A. C. A. de Vooys, G. L. Beltramo, B. van Riet, J. A. R. van Veen and M. T. M. Koper, *Electrochim. Acta*, 2004, **49**, 1307–1314.

32 Z. Li, L. Wang, Y. Cai, J.-R. Zhang and W. Zhu, *J. Hazard. Mater.*, 2022, **440**, 129828.

33 Z. Lyu, S. Ding, L. Fang, X. Li, T. Li, M. Xu, X. Pan, W. Zhu, Y. Zhou, D. Du and Y. Lin, *Anal. Chem.*, 2023, **95**, 4521–4528.

34 H. Wang, Q.-L. Zhu, R. Zou and Q. Xu, *Chem*, 2017, **2**, 52–80.

35 K. Li, Y. Cai, X. Yang, S. Wang, C. Teng, Y. Tian, Q. Min and W. Zhu, *Adv. Funct. Mater.*, 2022, **32**, 2113002.

36 H. Du, J. Fu, L.-X. Liu, S. Ding, Z. Lyu, Y.-C. Chang, X. Jin, F. O. Kengara, B. Song, Q. Min, J.-J. Zhu, D. Du, C. Gu, Y. Lin, J.-S. Hu and W. Zhu, *Mater. Today*, 2022, **59**, 182–199.

37 M. Jouny, J.-J. Lv, T. Cheng, B. H. Ko, J.-J. Zhu, W. A. Goddard and F. Jiao, *Nat. Chem.*, 2019, **11**, 846–851.

38 Y. Chai, Z. Lyu, H. Du, P. Li, S. Ding, Y. Jiang, H. Wang, Q. Min, D. Du, Y. Lin and W. Zhu, *SusMat*, 2022, **2**, 392–410.

39 X. Peng, L. Zeng, D. Wang, Z. Liu, Y. Li, Z. Li, B. Yang, L. Lei, L. Dai and Y. Hou, *Chem. Soc. Rev.*, 2023, **52**, 2193–2237.

40 H. Wang, Y. Jiang, S. Li, F. Gou, X. Liu, Y. Jiang, W. Luo, W. Shen, R. He and M. Li, *Appl. Catal., B*, 2022, **318**, 121819.

41 C. Lv, L. Zhong, H. Liu, Z. Fang, C. Yan, M. Chen, Y. Kong, C. Lee, D. Liu, S. Li, J. Liu, L. Song, G. Chen, Q. Yan and G. Yu, *Nat. Sustain.*, 2021, **4**, 868–876.

42 J.-A. Lai, Z. Zhang, X. Yang and Y. Zhang, *Innov. Mater.*, 2023, **1**, 100020.

43 Y. Shi and B. Zhang, *Chem. Soc. Rev.*, 2016, **45**, 1529–1541.

44 M. Jitaru, D. A. Lowy, M. Toma, B. C. Toma and L. Oniciu, *J. Appl. Electrochem.*, 1997, **27**, 875–889.

45 Y. Wang, W. Zhou, R. Jia, Y. Yu and B. Zhang, *Angew. Chem., Int. Ed.*, 2020, **59**, 5350–5354.

46 C. Ma, H.-F. Wei, M.-X. Wang, S. Wu, Y.-C. Chang, J. Zhang, L.-P. Jiang, W. Zhu, Z. Chen and Y. Lin, *Nano Lett.*, 2020, **20**, 5008–5016.

47 S. Guo, X. Zhang, W. Zhu, K. He, D. Su, A. Mendoza-Garcia, S. F. Ho, G. Lu and S. Sun, *J. Am. Chem. Soc.*, 2014, **136**, 15026–15033.

48 H. Tian, W. Zhu, Q. Shi, S. Ding, Z. Lyu, M. Xu, X. Pan, M. H. Engelhard, D. Dan and Y. Lin, *J. Mater. Chem. A*, 2022, **10**, 11196–11204.

49 H. Lv, Z. Xi, Z. Chen, S. Guo, Y. Yu, W. Zhu, Q. Li, X. Zhang, M. Pan, G. Lu, S. Mu and S. Sun, *J. Am. Chem. Soc.*, 2015, **137**, 5859–5862.

50 G. Wang, X. Li, X. Yang, L.-X. Liu, Y. Cai, Y. Wu, S. Wang, H. Li, Y. Zhou, Y. Wang and Y. Zhou, *Chem. – Eur. J.*, 2022, **28**, e202201834.

51 M. Shibata and N. Furuya, *J. Electroanal. Chem.*, 2001, **507**, 177–184.

52 J. He, N. J. J. Johnson, A. Huang and C. P. Berlinguette, *ChemSusChem*, 2018, **11**, 48–57.

53 K. Chen, M. Cao, G. Ni, S. Chen, H. Liao, L. Zhu, H. Li, J. Fu, J. Hu, E. Cortés and M. Liu, *Appl. Catal., B*, 2022, **306**, 121093.

54 J. Wang, Y. Wang, C. Cai, Y. Liu, D. Wu, M. Wang, M. Li, X. Wei, M. Shao and M. Gu, *Nano Lett.*, 2023, **23**, 1897–1903.

55 T. Hou, J. Ding, H. Zhang, S. Chen, Q. Liu, J. Luo and X. Liu, *Mater. Chem. Front.*, 2023, **7**, 4952–4960.

56 S. Liu, S. Yin, Z. Wang, Y. Xu, X. Li, L. Wang and H. Wang, *Cell Rep. Phys. Sci.*, 2022, **3**, 100869.

57 Y. Feng, H. Yang, Y. Zhang, X. Huang, L. Li, T. Cheng and Q. Shao, *Nano Lett.*, 2020, **20**, 8282–8289.

58 S. Kim, J. Park, J. Hwang and J. Lee, *EnergyChem*, 2021, **3**, 100054.

59 Y. Liu and W. Zhang, *Commun. Chem.*, 2023, **6**, 36.

60 J. Liu, Y. Cai, R. Song, S. Ding, Z. Lyu, Y.-C. Chang, H. Tian, X. Zhang, D. Du, W. Zhu, Y. Zhou and Y. Lin, *Mater. Today*, 2021, **48**, 95–114.

61 L. Wang, W. Chen, D. Zhang, Y. Du, R. Amal, S. Qiao, J. Wu and Z. Yin, *Chem. Soc. Rev.*, 2019, **48**, 5310–5349.

62 Z. Li, Y. Chen, S. Ji, Y. Tang, W. Chen, A. Li, J. Zhao, Y. Xiong, Y. Wu, Y. Gong, T. Yao, W. Liu, L. Zheng, J. Dong, Y. Wang, Z. Zhuang, W. Xing, C.-T. He, C. Peng, W.-C. Cheong, Q. Li, M. Zhang, Z. Chen, N. Fu, X. Gao, W. Zhu, J. Wan, J. Zhang, L. Gu, S. Wei, P. Hu, J. Luo, J. Li, C. Chen, Q. Peng, X. Duan, Y. Huang, X.-M. Chen, D. Wang and Y. Li, *Nat. Chem.*, 2020, **12**, 764–772.

63 X. Xie, C. He, B. Li, Y. He, D. A. Cullen, E. C. Wegener, A. J. Kropf, U. Martinez, Y. Cheng, M. H. Engelhard, M. E. Bowden, M. Song, T. Lemmon, X. S. Li, Z. Nie, J. Liu, D. J. Myers, P. Zelenay, G. Wang, G. Wu, V. Ramani and Y. Shao, *Nat. Catal.*, 2020, **3**, 1044–1054.

64 M. Li, H. Wang, W. Luo, P. C. Sherrell, J. Chen and J. Yang, *Adv. Mater.*, 2020, **32**, 2001848.

65 J. Leverett, T. Tran-Phu, J. A. Yuwono, P. Kumar, C. Kim, Q. Zhai, C. Han, J. Qu, J. Cairney, A. N. Simonov, R. K. Hocking, L. Dai, R. Daiyan and R. Amal, *Adv. Energy Mater.*, 2022, **12**, 2201500.

66 X. Wei, Y. Liu, X. Zhu, S. Bo, L. Xiao, C. Chen, T. T. T. Nga, Y. He, M. Qiu, C. Xie, D. Wang, Q. Liu, F. Dong, C.-L. Dong, X.-Z. Fu and S. Wang, *Adv. Mater.*, 2023, **35**, 2300020.

67 N. Wang, Z. Liu, J. Ma, J. Liu, P. Zhou, Y. Chao, C. Ma, X. Bo, J. Liu, Y. Hei, Y. Bi, M. Sun, M. Cao, H. Zhang, F. Chang, H.-L. Wang, P. Xu, Z. Hu, J. Bai, H. Sun, G. Hu and M. Zhou, *ACS Sustainable Chem. Eng.*, 2020, **8**, 13813–13822.

68 X. Liu, Z. Wang, Y. Tian and J. Zhao, *J. Phys. Chem. C*, 2020, **124**, 3722–3730.

69 R. Boppella, M. Austeria P, Y. Kim, E. Kim, I. Song, Y. Eom, D. P. Kumar, M. Balamurµgan, E. Sim, D. H. Kim and T. K. Kim, *Adv. Funct. Mater.*, 2022, **32**, 2202351.

70 Z. Geng, Y. Liu, X. Kong, P. Li, K. Li, Z. Liu, J. Du, M. Shu, R. Si and J. Zeng, *Adv. Mater.*, 2018, **30**, 1870301.

71 D. Jiao, Y. Liu, Q. Cai and J. Zhao, *J. Mater. Chem. A*, 2021, **9**, 1240–1251.

72 H. Zou, L. J. Arachchige, W. Rong, C. Tang, R. Wang, S. Tan, H. Chen, D. He, J. Hu, E. Hu, C. Sun and L. Duan, *Adv. Funct. Mater.*, 2022, **32**, 2200333.

73 Y. Hu, Z. Li, B. Li and C. Yu, *Small*, 2022, **18**, 2203589.

74 R. Li and D. Wang, *Adv. Energy Mater.*, 2022, **12**, 2103564.

75 J. Liu, S. C. Smith, Y. Gu and L. Kou, *Adv. Funct. Mater.*, 2023, **33**, 2305894.

76 X. Zhang, X. Zhu, S. Bo, C. Chen, M. Qiu, X. Wei, N. He, C. Xie, W. Chen, J. Zheng, P. Chen, S. P. Jiang, Y. Li, Q. Liu and S. Wang, *Nat. Commun.*, 2022, **13**, 5337.

77 C. Liu, H. Tong, P. Wang, R. Huang, P. Huang, G. Zhou and L. Liu, *Appl. Catal., B*, 2023, **336**, 122917.

78 H. Yang, Y. Chen and Y. Qin, *Chin. J. Catal.*, 2020, **41**, 227–241.

79 S. Tian, Q. Fu, W. Chen, Q. Feng, Z. Chen, J. Zhang, W.-C. Cheong, R. Yu, L. Gu, J. Dong, J. Luo, C. Chen, Q. Peng, C. Draxl, D. Wang and Y. Li, *Nat. Commun.*, 2018, **9**, 2353.

80 Z. Lu, B. Wang, Y. Hu, W. Liu, Y. Zhao, R. Yang, Z. Li, J. Luo, B. Chi, Z. Jiang, M. Li, S. Mu, S. Liao, J. Zhang and X. Sun, *Angew. Chem., Int. Ed.*, 2019, **58**, 2622–2626.

81 J. Wang, Z. Huang, W. Liu, C. Chang, H. Tang, Z. Li, W. Chen, C. Jia, T. Yao, S. Wei, Y. Wu and Y. Li, *J. Am. Chem. Soc.*, 2017, **139**, 17281–17284.

82 H. Zhou, B. Xiong, L. Chen and J. Shi, *J. Mater. Chem. A*, 2020, **8**, 20286–20293.

83 K. Zhu, F. Shi, X. Zhu and W. Yang, *Nano Energy*, 2020, **73**, 104761.

84 L. Zhang, X.-Y. Xie, H. Wang, L. Ji, Y. Zhang, H. Chen, T. Li, Y. Luo, G. Cui and X. Sun, *Chem. Commun.*, 2019, **55**, 4627–4630.

85 C. Lv, C. Lee, L. Zhong, H. Liu, J. Liu, L. Yang, C. Yan, W. Yu, H. H. Hng, Z. Qi, L. Song, S. Li, K. P. Loh, Q. Yan and G. Yu, *ACS Nano*, 2022, **16**, 8213–8222.

86 X. Wei, X. Wen, Y. Liu, C. Chen, C. Xie, D. Wang, M. Qiu, N. He, P. Zhou, W. Chen, J. Cheng, H. Lin, J. Jia, X.-Z. Fu and S. Wang, *J. Am. Chem. Soc.*, 2022, **144**, 11530–11535.

87 N. Meng, Y. Huang, Y. Liu, Y. Yu and B. Zhang, *Cell Rep. Phys. Sci.*, 2021, **2**, 100378.

88 D. Raciti and C. Wang, *ACS Energy Lett.*, 2018, **3**, 1545–1556.

89 N. Cao, Y. Quan, A. Guan, C. Yang, Y. Ji, L. Zhang and G. Zheng, *J. Colloid Interface Sci.*, 2020, **577**, 109–114.

90 X. Yang, K. Sun, M. Ma, C. Xu, R. Ren, J. Qiao, Z. Wang, S. Zhen, R. Hou and W. Sun, *Appl. Catal., B*, 2020, **272**, 118968.

91 Z. Chen, T. Fan, Y.-Q. Zhang, J. Xiao, M. Gao, N. Duan, J. Zhang, J. Li, Q. Liu, X. Yi and J.-L. Luo, *Appl. Catal., B*, 2020, **261**, 118243.

92 K. Wang, S. Shu, M. Chen, J. Li, K. Zhou, J. Pan, X. Wang, X. Li, J. Sheng, F. Dong and G. Jiang, *Chem. Eng. J.*, 2020, **381**, 122673.

93 Q. Wu, M.-J. Mao, Q.-J. Wu, J. Liang, Y.-B. Huang and R. Cao, *Small*, 2021, **17**, 2004933.

94 M. Yuan, J. Chen, Y. Bai, Z. Liu, J. Zhang, T. Zhao, Q. Wang, S. Li, H. He and G. Zhang, *Angew. Chem., Int. Ed.*, 2021, **60**, 10910–10918.

95 M. Yuan, J. Chen, Y. Bai, Z. Liu, J. Zhang, T. Zhao, Q. Shi, S. Li, X. Wang and G. Zhang, *Chem. Sci.*, 2021, **12**, 6048–6058.

96 G. Li, Y. Li, H. Liu, Y. Guo, Y. Li and D. Zhu, *Chem. Commun.*, 2010, **46**, 3256–3258.

97 Y. Fang, Y. Liu, L. Qi, Y. Xue and Y. Li, *Chem. Soc. Rev.*, 2022, **51**, 2681–2709.

98 D. Zhang, Y. Xue, X. Zheng, C. Zhang and Y. Li, *Natl. Sci. Rev.*, 2023, **10**, nwac209.

99 M.-Y. Li, Y. Shi, C.-C. Cheng, L.-S. Lu, Y.-C. Lin, H.-L. Tang, M.-L. Tsai, C.-W. Chu, K.-H. Wei, J.-H. He, W.-H. Chang, K. Suenaga and L.-J. Li, *Science*, 2015, **349**, 524–528.

100 Z. Huang, X. Tang, J. Zhao, H. Lin, M. Nie and Q. Li, *J. Mater. Chem. C*, 2022, **10**, 3489–3499.

101 B. Qiu, C. Wang, N. Zhang, L. Cai, Y. Xiong and Y. Chai, *ACS Catal.*, 2019, **9**, 6484–6490.

102 W. D. Chemelewski, J. R. Rosenstock and C. B. Mullins, *J. Mater. Chem. A*, 2014, **2**, 14957–14962.

103 Z. Ye, T. Li, G. Ma, Y. Dong and X. Zhou, *Adv. Funct. Mater.*, 2017, **27**, 1704083.

104 Z. Li, X. Lu, J. Teng, Y. Zhou and W. Zhuang, *Nanoscale*, 2021, **13**, 11314–11324.

105 B. Zhang, L. Sun, Y. Wang, S. Chen and J. Zhang, *J. Energy Chem.*, 2020, **41**, 7–14.

106 W. Lee, G. M. Kim, S. Baik and J. W. Lee, *Electrochim. Acta*, 2016, **210**, 743–753.

107 W. Ni, Y. Xue, X. Zang, C. Li, H. Wang, Z. Yang and Y.-M. Yan, *ACS Nano*, 2020, **14**, 2014–2023.

108 X. Liu, P. V. Kumar, Q. Chen, L. Zhao, F. Ye, X. Ma, D. Liu, X. Chen, L. Dai and C. Hu, *Appl. Catal., B*, 2022, **316**, 121618.

109 D. Jiao, Y. Dong, X. Cui, Q. Cai, C. R. Cabrera, J. Zhao and Z. Chen, *J. Mater. Chem. A*, 2023, **11**, 232–240.

110 C. Zhu, C. Wen, M. Wang, M. Zhang, Y. Geng and Z. Su, *Chem. Sci.*, 2022, **13**, 1342–1354.

111 D. Xu, S.-N. Zhang, J.-S. Chen and X.-H. Li, *Chem. Rev.*, 2023, **123**, 1–30.

112 Z. Li, M. Hu, P. Wang, J. Liu, J. Yao and C. Li, *Coord. Chem. Rev.*, 2021, **439**, 213953.

113 Y. Hori, H. Wakebe, T. Tsukamoto and O. Koga, *Surf. Sci.*, 1995, **335**, 258–263.

114 Z. Niu, W. D. C. B. Gunatilleke, Q. Sun, P. C. Lan, J. Perman, J.-G. Ma, Y. Cheng, B. Aguila and S. Ma, *Chem*, 2018, **4**, 2587–2599.

115 J. Li, Z. Xia, Q. Xue, M. Zhang, S. Zhang, H. Xiao, Y. Ma and Y. Qu, *Small*, 2021, **17**, 2103018.

116 M. Yuan, J. Chen, Y. Xu, R. Liu, T. Zhao, J. Zhang, Z. Ren, Z. Liu, C. Streb, H. He, C. Yang, S. Zhang and G. Zhang, *Energy Environ. Sci.*, 2021, **14**, 6605–6615.

117 H. Hu, J. Wang, P. Tao, C. Song, W. Shang, T. Deng and J. Wu, *J. Mater. Chem. A*, 2022, **10**, 5835–5849.

118 L. Zhang, W. Shi and B. Zhang, *J. Energy Chem.*, 2017, **26**, 1117–1135.

119 J. E. Kim, J. H. Jang, K. M. Lee, M. Balamurugan, Y. I. Jo, M. Y. Lee, S. Choi, S. W. Im and K. T. Nam, *Angew. Chem., Int. Ed.*, 2021, **60**, 21943–21951.

120 N. Meng, J. Shao, H. Li, Y. Wang, X. Fu, C. Liu, Y. Yu and B. Zhang, *Nat. Commun.*, 2022, **13**, 5452.

121 Y. Luo, K. Xie, P. Ou, C. Lavallais, T. Peng, Z. Chen, Z. Zhang, N. Wang, X.-Y. Li, I. Grigioni, B. Liu, D. Sinton, J. B. Dunn and E. H. Sargent, *Nat. Catal.*, 2023, **6**, 939–948.

122 Y. Zhao, Y. Ding, W. Li, C. Liu, Y. Li, Z. Zhao, Y. Shan, F. Li, L. Sun and F. Li, *Nat. Commun.*, 2023, **14**, 4491.

123 H. Sun and W. Zhou, *Energy Fuels*, 2021, **35**, 5716–5737.

124 M. Wang, L. Árnadóttir, Z. J. Xu and Z. Feng, *Nano-Micro Lett.*, 2019, **11**, 47.

125 Y. Mao, Y. Jiang, Q. Gou, S. Lv, Z. Song, Y. Jiang, W. Wang, M. Li, L. Zheng, W. Su and R. He, *Appl. Catal., B*, 2024, **340**, 123189.

126 C. Chen, X. Yan, Y. Wu, S. Liu, X. Sun, Q. Zhu, R. Feng, T. Wu, Q. Qian, H. Liu, L. Zheng, J. Zhang and B. Han, *Chem. Sci.*, 2021, **12**, 5938–5943.

127 H. Zhang, Z. Zhou, Q. Lei and T. W. B. Lo, *Curr. Opin. Electrochem.*, 2023, **38**, 101215.

128 K. Feng, H. Zhang, J. Gao, J. Xu, Y. Dong, Z. Kang and J. Zhong, *Appl. Phys. Lett.*, 2020, 116.

129 Z. Liang, L. Yin, H. Yin, Z. Yin and Y. Du, *Nanoscale Horiz.*, 2022, **7**, 31–40.

130 C. Chen, N. He and S. Wang, *Small Sci.*, 2021, **1**, 2100070.

131 Z. Sun, T. Ma, H. Tao, Q. Fan and B. Han, *Chem*, 2017, **3**, 560–587.

132 J. Liu, L. Peng, Y. Zhou, L. Lv, J. Fu, J. Lin, D. Guay and J. Qiao, *ACS Sustainable Chem. Eng.*, 2019, **7**, 15739–15746.

133 P. Senthilkumar, M. Mohapatra and S. Basu, *RSC Adv.*, 2022, **12**, 1287–1309.

134 F.-Y. Chen, Z.-Y. Wu, Z. Adler and H. Wang, *Joule*, 2021, **5**, 1704–1731.

135 D. Li, N. Xu, Y. Zhao, C. Zhou, L.-P. Zhang, L.-Z. Wu and T. Zhang, *Small Methods*, 2022, **6**, 2200561.

136 D. Saravanakumar, J. Song, S. Lee, N. H. Hur and W. Shin, *ChemSusChem*, 2017, **10**, 3999–4003.

137 J. J. Mccarthy, *Limnol. Oceanogr.*, 1970, **15**, 309–313.

138 Y. Zhao, R. Shi, X. Bian, C. Zhou, Y. Zhao, S. Zhang, F. Wu, G. I. N. Waterhouse, L.-Z. Wu, C.-H. Tung and T. Zhang, *Adv. Sci.*, 2019, **6**, 1802109.

139 P. S. Francis, S. W. Lewis and K. F. Lim, *TrAC, Trends Anal. Chem.*, 2002, **21**, 389–400.

140 S. Kodama and T. Suzuki, *J. Food Sci.*, 1995, **60**, 1097–1099.

141 D. Li, N. Xu, Y. Zhao, R. Shi, C. Zhou, L.-P. Zhang and T. Zhang, *Adv. Energy Mater.*, 2023, 2303885.

142 T. Yuan and O. Voznyy, *Cell Rep. Phys. Sci.*, 2023, **4**, 101521.

143 J. Mukherjee, S. Paul, A. Adalder, S. Kapse, R. Thapa, S. Mandal, B. Ghorai, S. Sarkar and U. K. Ghorai, *Adv. Funct. Mater.*, 2022, **32**, 2200882.

144 Z. Lv, S. Zhou, L. Zhao, Z. Liu, J. Liu, W. Xu, L. Wang and J. Lai, *Adv. Energy Mater.*, 2023, **13**, 2300946.

145 J. Geng, S. Ji, M. Jin, C. Zhang, M. Xu, G. Wang, C. Liang and H. Zhang, *Angew. Chem., Int. Ed.*, 2023, **62**, e202210958.

146 J. Qin, N. Liu, L. Chen, K. Wu, Q. Zhao, B. Liu and Z. Ye, *ACS Sustainable Chem. Eng.*, 2022, **10**, 15869–15875.

147 Y. Wang, S. Xia, J. Zhang, Z. Li, R. Cai, C. Yu, Y. Zhang, J. Wu and Y. Wu, *ACS Energy Lett.*, 2023, **8**, 3373–3380.

148 X. Tu, X. Zhu, S. Bo, X. Zhang, R. Miao, G. Wen, C. Chen, J. Li, Y. Zhou, Q. Liu, D. Chen, H. Shao, D. Yan, Y. Li, J. Jia and S. Wang, *Angew. Chem., Int. Ed.*, 2024, **63**, e202317087.

149 M. Qiu, X. Zhu, S. Bo, K. Cheng, N. He, K. Gu, D. Song, C. Chen, X. Wei, D. Wang, Y. Liu, S. Li, X. Tu, Y. Li, Q. Liu, C. Li and S. Wang, *CCS Chem.*, 2023, **5**, 2617–2627.

150 J. Fu, Y. Yang and J.-S. Hu, *ACS Mater. Lett.*, 2021, **3**, 1468–1476.

151 N. Meng, X. Ma, C. Wang, Y. Wang, R. Yang, J. Shao, Y. Huang, Y. Xu, B. Zhang and Y. Yu, *ACS Nano*, 2022, **16**, 9095–9104.

152 Y. Chen, Y. Liu, S. Hu, D. Wu, M. Zhang and Z. Cheng, *Sci. Total Environ.*, 2024, **913**, 169722.

153 D. Anastasiadou, B. Ligt, Y. He, R. C. J. van de Poll, J. F. M. Simons and M. C. Figueiredo, *Commun. Chem.*, 2023, **6**, 199.

154 X. Cao, D. Tan, B. Wulan, K. S. Hui, K. N. Hui and J. Zhang, *Small Methods*, 2021, **5**, 2100700.

155 A. M. Tripathi, W.-N. Su and B. J. Hwang, *Chem. Soc. Rev.*, 2018, **47**, 736–851.

156 Y. J. Wang, D. W. Chen, C. Chen and S. Y. Wang, *Acc. Chem. Res.*, 2024, **57**, 247–256.

157 Y. Yu, B. Mao, A. Geller, R. Chang, K. Gaskell, Z. Liu and B. W. Eichhorn, *Phys. Chem. Chem. Phys.*, 2014, **16**, 11633–11639.

158 E. L. Clark, M. R. Singh, Y. Kwon and A. T. Bell, *Anal. Chem.*, 2015, **87**, 8013–8020.

159 S. Jia, S. Matsuda, S. Tamura, S. Shironita and M. Umeda, *Electrochim. Acta*, 2018, **261**, 340–345.

160 P. Čičmanec, R. Bulánek and K. Frolich, *J. Therm. Anal. Calorim.*, 2011, **105**, 837–844.

161 M. Zheng, H. Ma, Z. Li, H. Yu, L. Nie, C. Ye, X. Chen and J. Wang, *Appl. Catal., B*, 2024, **342**, 123366.

162 M. Shibata, K. Yoshida and N. Furuya, *J. Electrochem. Soc.*, 1998, **145**, 595.

163 M. Shibata, K. Yoshida and N. Furuya, *J. Electrochem. Soc.*, 1998, **145**, 2348.

164 Y.-G. Zhou, Y. Kang and J. Huang, *CCS Chem.*, 2020, **2**, 31–41.

165 V. Hessel, N. N. Tran, M. R. Asrami, Q. D. Tran, N. V. D. Long, M. Escribà-Gelonch, J. O. Tejada, S. Linke and K. Sundmacher, *Green Chem.*, 2022, **24**, 410–437.

166 B. Chang, H. Pang, F. Raziq, S. Wang, K.-W. Huang, J. Ye and H. Zhang, *Energy Environ. Sci.*, 2023, **16**, 4714–4758.

167 Y. Ji, A. Guan and G. Zheng, *Cell Rep. Phys. Sci.*, 2022, **3**, 101072.

168 M. Jiang, M. Zhu, M. Wang, Y. He, X. Luo, C. Wu, L. Zhang and Z. Jin, *ACS Nano*, 2023, **17**, 3209–3224.

169 B. Min, Q. Gao, Z. Yan, X. Han, K. Hosmer, A. Campbell and H. Zhu, *Ind. Eng. Chem. Res.*, 2021, **60**, 14635–14650.

170 F. Liu, C. Shi, X. Guo, Z. He, L. Pan, Z.-F. Huang, X. Zhang and J.-J. Zou, *Adv. Sci.*, 2022, **9**, 2200307.

171 Y. Huang, Y. Wang, Y. Wu, Y. Yu and B. Zhang, *Sci. China: Chem.*, 2022, **65**, 204–206.

172 M. Eisa, D. Ragauskaitė, S. Adhikari, F. Bella and J. Baltrusaitis, *ACS Sustainable Chem. Eng.*, 2022, **10**, 8997–9001.

173 G. Gianola, R. Speranza, F. Bella and A. Lamberti, *Sol. Energy*, 2023, **265**, 112116.

174 I. Ali, M. R. Islam, J. Yin, S. J. Eichhorn, J. Chen, N. Karim and S. Afroj, *ACS Nano*, 2024, **18**, 3871–3915.

175 H. Gao, K. Xiao, R. Lin, S. Zhao, W. Wang, S. Dayneko, C. Duan, C. Ji, H. Sun, A. D. Bui, C. Liu, J. Wen, W. Kong, H. Luo, X. Zheng, Z. Liu, H. Nguyen, J. Xie, L. Li, M. I. Saidaminov and H. Tan, *Science*, 2024, **383**, 855–859.

176 R. Lin, Y. Wang, Q. Lu, B. Tang, J. Li, H. Gao, Y. Gao, H. Li, C. Ding, J. Wen, P. Wu, C. Liu, S. Zhao, K. Xiao, Z. Liu, C. Ma, Y. Deng, L. Li, F. Fan and H. Tan, *Nature*, 2023, **620**, 994–1000.

177 X. Zhang, Y. Tian, L. Chen, X. Hu and Z. Zhou, *J. Phys. Chem. Lett.*, 2022, **13**, 7920–7930.

178 S. N. Steinmann, Q. Wang and Z. W. Seh, *Mater. Horiz.*, 2023, **10**, 393–406.

179 S. Shin, S. Sultan, Z.-X. Chen, H. Lee, H. Choi, T.-U. Wi, C. Park, T. Kim, C. Lee, J. Jeong, H. Shin, T.-H. Kim, H. Ju, H. C. Yoon, H.-K. Song, H.-W. Lee, M.-J. Cheng and Y. Kwon, *Energy Environ. Sci.*, 2023, **16**, 2003–2013.

180 Z. Mei, Y. Zhou, W. Lv, S. Tong, X. Yang, L. Chen and N. Zhang, *ACS Sustainable Chem. Eng.*, 2022, **10**, 12477–12496.

181 L. Hu, Z. Xing and X. Feng, *ACS Energy Lett.*, 2020, **5**, 430–436.

182 Y. Zhong, H. Xiong, J. Low, R. Long and Y. Xiong, *eScience*, 2023, **3**, 100086.

183 P. Xu, X. Li, Y. Zhou, Y. Chen, X. Wang, H. Jia, M. Li, H. Yu and X. Li, *J. Phys. Chem. Lett.*, 2023, **14**, 567–575.